

A PHYSICAL-NUMERICAL MODEL FOR THE PREDICTION OF SYNOPTIC-SCALE LOW CLOUDINESS

JOSEPH P. GERRITY, JR.

The Travelers Research Center, Inc., 250 Constitution Plaza, Hartford, Conn.

ABSTRACT

A system of equations governing the behavior of a physical model of the atmospheric, planetary boundary layer was formulated for solution on a digital computer. The physical-numerical model was designed to permit the investigation of the significance of certain boundary-layer processes for the development of horizontally extensive areas of low cloudiness.

Numerical solutions of the equations were computed for three synoptic cases. In each case, the forecast period was 12 hr. The initial state of the atmosphere was analyzed from synoptic surface and upper-air observations in the eastern United States. The computations were made for a finite difference grid with 1200 grid points, using a 15-min. time step. The vertical coordinate was defined by 12 grid points over each of 100 grid points in the horizontal plane. The average spacing of the horizontal grid points was 160 km. The separation of the vertical grid points expanded from 50 m. near the ground to 450 m. at the uppermost level.

The model boundary layer was subdivided into a 50-m. deep, surface contact layer and a 1950-m. deep, transition layer. Stability-dependent, constant-flux profile formulas were applied within the surface contact layer. These were used in conjunction with semi-empirical formulas to derive boundary conditions applicable at the base of the transition layer. Observed data were used to prescribe the horizontal pressure gradient force at the upper boundary of the transition layer. Within the transition layer the horizontal wind was computed by means of a diagnostic equation implying a balance of the Coriolis, pressure gradient, and eddy viscous forces. The eddy viscosity coefficient was held equal to its value at the top of the surface contact layer. The pressure gradient force was assumed to be a linear function of height; its variation was computed from the predicted temperature field. The eddy conductivity and diffusivity coefficients were assumed to be equal. They were computed as functions of the stability.

The results obtained in one of the synoptic case studies is presented in some detail. Certain statistics are presented for all three cases studied. It is concluded that, despite certain deficiencies, the model seems capable of improving the accuracy of low-cloud predictions for data-dense regions. It is also suggested that the model may have diagnostic and predictive utility for other applications which require a knowledge of the structure of the atmosphere within the planetary boundary layer.

CONTENTS

	Page
1. INTRODUCTION.....	261
2. DERIVATION OF MODEL EQUATIONS.....	262
Coordinate System and Fundamental Equations.....	262
Model Equations for the Transition Layer.....	263
Model Equations for the Layer of Constant Flux.....	265
3. COMPUTATIONAL MODEL.....	269
Computational Form of Model Equations.....	269
Analysis of Data.....	271
4. RESULTS OF NUMERICAL EXPERIMENTS.....	271
5. CONCLUSIONS.....	280
ACKNOWLEDGMENTS.....	281
REFERENCES.....	281

1. INTRODUCTION

One of the more important requirements imposed upon the meteorological services by modern aviation operations is the accurate prediction of the development, movement, and decay of horizontally extensive regions of low cloudiness. In a review of the status of numerical methods for

cloud prediction (Arnason, Gerrity, and Pavlowitz [1]), it became clear that the methods studied possessed a number of deficiencies which might well be responsible for their failure to provide useful prediction of low cloudiness. The major deficiencies in the techniques seemed to be the inadequacy of the vertical resolution of the data employed and the neglect of the physical processes which are active in the atmospheric boundary layer.

We therefore undertook the formulation and analysis of a physical-numerical cloud prediction model in which emphasis would be placed upon the description of boundary layer processes. Limitations imposed by the nature of the available observational data and by the storage capacity of the high-speed computer, necessitated the omission, or approximate evaluation, of certain physical processes in designing the model.

Three case studies were carried out with the model. The synoptic situations differed in each case, but had in common the occurrence of extensive regions of low cloudiness. In each case, the forecast interval was restricted to 12 hr. because of the limited horizontal extent of the

geographical region for which data could be stored within the high-speed computer memory. The analysis of the results obtained in these forecasts assesses the accuracy of the predictions and the significance in each case of the boundary layer processes.

In formulating the boundary layer model, we were able to employ methods which are similar in some respects to those used by Estoque [7], Fisher and Caplan [8], and Pandolfo, Cooley, and Atwater [23]. These investigators have emphasized the small-scale structure of the boundary layer. Their work is appropriate to short-period forecasts valid at the middle of a well-instrumented sub-synoptic observational network.

The most significant physical simplifications used in deriving the model involve the treatment of the wind field and of the radiational heat transfer.

Motivated by consideration of both observational inaccuracy and mathematical difficulty, we replaced the horizontal equations of motion by two kinematic balance equations. Throughout the bulk of the boundary layer, a balance of the Coriolis, pressure gradient, and frictional forces is assumed. Within a shallow layer next to the ground, the eddy flux of momentum is assumed to balance the surface stress. The latter approximation is equivalent to the assumption of a vertically constant value of the flux of momentum. The evaluation of the surface stress is made using the empirical relationship between the surface Rossby number and the stress developed by Lettau [17].

Results obtained by Elliott and Stevens [6] showed that, in the absence of clouds, the temperature change produced by convergence of the radiative heat flux is negligible except very close to the ground. Our treatment of the heat transfer by eddy motion involves the approximation that near the ground the eddy flux of heat does not vary with height. It seems therefore to be consistent to neglect the physical approach to computing radiative cooling near the ground. Instead, an empirical method for estimating the rate of temperature change at the level of the instrument shelter is used. This method provides a means for estimating the integrated effect of convergence of both radiative and eddy heat fluxes.

The neglect of radiative cooling at cloud surfaces and, for that matter, the neglect of the precipitation phase of the water transfer with the attendant cooling resulting from its evaporation are two shortcomings of the present model which we would like to have removed. However, the present version of the model fully occupied the high-speed memory of the available computer (IBM 7094-DCS). The reformulation, reprogramming, and increase in running time necessary to include these processes would have carried the research beyond its practical scope.

This research was initiated with the intention of utilizing a simple model. In particular, it was desired to use a formulation of the eddy transfer of heat and vapor which would not be disproportionate in its complexity to the method adopted for evaluating the horizontal and vertical components of the wind. Thus the initial computations

were made using the assumptions that: the mixing coefficient and eddy flux at the base of the transition layer could be computed from the laws valid for near-neutral conditions; the surface temperature and humidity could be held constant during the forecast period; the mixing coefficients were linearly decreasing functions of height through the transition layer. The results of these initial numerical experiments led us to reject each of these approximations in the final version of the model. The complexity of the model formulation of the eddy transfer process should therefore be regarded as having been imposed upon us by the characteristic evolution of real atmospheric data.

2. DERIVATION OF THE MODEL EQUATIONS

COORDINATE SYSTEM AND THE FUNDAMENTAL EQUATIONS

The coordinate system employed in the model equations was chosen to facilitate the application of boundary conditions. If r_e , ϕ , and λ are spherical coordinates fixed in the rotating earth (see Haurwitz [14]), we may define the model coordinates, x , y , and z , by the equations

$$x = am(\phi) \cos \phi \cos \lambda, \quad (2.1)$$

$$y = am(\phi) \cos \phi \sin \lambda, \quad (2.2)$$

$$z = r_e - a - E(x, y). \quad (2.3)$$

In these equations, a is the mean radius of the earth and $E(x, y)$ is the elevation of the terrain above mean sea level. The polar stereographic map scale factor is denoted by $m(\phi)$.

The planetary boundary layer is assumed to occupy the region between $z=0$ and $z=H$ ($H=2$ km.). A subdivision of the boundary layer is defined by letting the region between $z=0$ and $z=h$ ($h=50$ m.) be denoted as the layer of constant flux and the remainder ($h \leq z \leq H$) be denoted as the transition layer.

We will next write the fundamental equations used in deriving the model employing the x, y, z coordinate system. First, it should be pointed out that, in transforming the equations from spherical coordinates, one must account for the dependence of z upon x and y through the function $E(x, y)$. The method for accomplishing such a transformation is given in Haltiner and Martin [13] and other texts. In the following equations, the hydrostatic approximation was used and the following have been neglected: (a) all terms involving the vertical velocity (except for the vertical derivative of w in the continuity equation) which are not part of the individual derivative; and (b) all terms associated with the variability of the map scale factor, $m(\phi)$, or the convergence of the meridians. The equations are:

$$\frac{du}{dt} - fv = -\frac{m}{\rho} \left[\frac{\partial p}{\partial x} + \rho g \frac{\partial E}{\partial x} \right] + \frac{\partial}{\partial z} \left[K_M \frac{\partial u}{\partial z} \right] \quad (2.4)$$

$$\frac{dv}{dt} + fu = -\frac{m}{\rho} \left[\frac{\partial p}{\partial y} + \rho g \frac{\partial E}{\partial y} \right] + \frac{\partial}{\partial z} \left[K_M \frac{\partial v}{\partial z} \right] \quad (2.5)$$

$$\frac{\partial p}{\partial z} = -\rho g \quad (2.6)$$

$$\frac{dp}{dt} = -\rho \left[\frac{\partial w}{\partial z} + m \left(\frac{\partial u}{\partial x} + \frac{\partial v}{\partial y} \right) \right] \quad (2.7)$$

$$\frac{d\theta}{dt} = \frac{\partial}{\partial z} \left[K_H \frac{\partial \theta}{\partial z} \right] + \frac{\theta}{T} \frac{Q}{c_p} \quad (2.8)$$

$$\frac{dq}{dt} = -C + \frac{\partial}{\partial z} \left[K_V \frac{\partial q}{\partial z} \right] \quad (2.9)$$

$$\frac{dr}{dt} = \frac{\partial}{\partial z} \left[K_V \frac{\partial r}{\partial z} \right] \quad (2.10)$$

In these equations

$$u = \frac{dx}{dt} / m(\phi) \quad (2.11)$$

$$v = \frac{dy}{dt} / m(\phi) \quad (2.12)$$

$$w = \frac{dz}{dt} \quad (2.13)$$

and

$$\frac{d}{dt} () = \left[\frac{\partial}{\partial t} + m(\phi)u \frac{\partial}{\partial x} + m(\phi)v \frac{\partial}{\partial y} + w \frac{\partial}{\partial z} \right] () \quad (2.14)$$

The other symbols are defined as follows:

c_p	specific heat at constant pressure of dry air
f	Coriolis parameter
ρ	air density
p	air pressure
g	acceleration due to gravity
E	elevation of terrain above mean sea level
K_M	eddy viscosity
θ	potential temperature
K_H	eddy conductivity
T	air temperature
Q	rate of addition of heat per unit mass
q	specific humidity
C	rate of change of q due to condensation
K_V	eddy diffusivity
r	specific moisture (ratio of mass of water substance to mass of moist air in a unit volume).

The first two equations are the equations of motion in the surface of constant z . Equations (2.6) and (2.7) are the hydrostatic and continuity equations. The thermodynamic equation is given as (2.8). The equations governing water substance are given in equations (2.9) and (2.10) on the assumption that no precipitation occurs and that the vapor and clouds follow the motion of the air.

MODEL EQUATIONS FOR THE TRANSITION LAYER

Recall that the transition layer occupies the region $h \leq z \leq H$. Equations (2.4) and (2.5) are simplified by: (a) neglecting the individual derivatives, (b) assuming that K_M is not a function of z , and (c) assuming that the geostrophic wind components defined by

$$u_g = -\frac{m}{\rho f} \left[\frac{\partial p}{\partial y} + \rho g \frac{\partial E}{\partial y} \right] \quad (2.15)$$

$$v_g = +\frac{m}{\rho f} \left[\frac{\partial p}{\partial x} + \rho g \frac{\partial E}{\partial x} \right] \quad (2.16)$$

are the following linear functions of z ,

$$u_g = u_g^H + B(H - z) \quad (2.17)$$

$$v_g = v_g^H + C(H - z). \quad (2.18)$$

We define

$$\alpha \equiv \left[\frac{f}{2K_M} \right]^{1/2}. \quad (2.19)$$

The equations (2.4) and (2.5) may then be written

$$\frac{\partial^2 u}{\partial z^2} = -2\alpha^2(v - v_g) \quad (2.20)$$

$$\frac{\partial^2 v}{\partial z^2} = +2\alpha^2(u - u_g). \quad (2.21)$$

The solution to these equations may be obtained using the boundary conditions

$$\left. \begin{matrix} u \rightarrow u_g \\ v \rightarrow v_g \end{matrix} \right\} \text{ as } z \rightarrow \infty, \quad (2.22)$$

and

$$\left. \begin{matrix} u = U \\ v = V \end{matrix} \right\} \text{ at } z = h. \quad (2.23)$$

The first of these conditions yields a solution of simpler computational form than arises if one sets the boundary condition, $u = u_g$ and $v = v_g$, at finite height (e.g., at $z = H$). Furthermore, the solutions differ by only a negligible amount for realistic values of α . The lower boundary values, U and V , are provided by the wind profiles derived subsequently for the layer of constant flux. Similarly, the value of K_M will be held equal to its value computed at $z = h$ from the formulas applicable in the layer of constant flux. The solutions to (2.20) and (2.21) are

$$u = u_g + e^{-\alpha(z-h)} \{ [U - u_g^h] \cos [\alpha(z-h)] + [V - v_g^h] \sin [\alpha(z-h)] \} \quad (2.24)$$

and

$$v = v_g + e^{-\alpha(z-h)} \{ [V - v_g^h] \cos [\alpha(z-h)] - [U - u_g^h] \sin [\alpha(z-h)] \} \quad (2.25)$$

in which u_g^h and v_g^h are the values of u_g and v_g at $z = h$.

The geostrophic wind components, u_g^H and v_g^H , are to be evaluated at the top of the transition layer from predic-

tions made with free-air models. The coefficients B and C are to be computed from the predicted field of temperature. Using the procedure outlined in Haurwitz [14] and taking appropriate account of terrain height variation, we derive the following relations:

$$u_g = u_g^H + \left[\frac{H-z}{H-h} \right] \left[(u_g^H - \tilde{u}) \left(\frac{T_h - T_H}{T_H} \right) - \frac{mgT_h}{f} \int_h^H \frac{\partial}{\partial y} \left(\frac{1}{T} \right) dz \right] \quad (2.26)$$

$$v_g = v_g^H + \left[\frac{H-z}{H-h} \right] \left[(v_g^H - \tilde{v}) \left(\frac{T_h - T_H}{T_H} \right) + \frac{mgT_h}{f} \int_h^H \frac{\partial}{\partial x} \left(\frac{1}{T} \right) dz \right] \quad (2.27)$$

in which

$$\tilde{u} = -\frac{mg}{f} \frac{\partial E}{\partial y}, \quad (2.28)$$

and

$$\tilde{v} = +\frac{mg}{f} \frac{\partial E}{\partial x}. \quad (2.29)$$

T_h and T_H are respectively the temperatures at $z=h$ and $z=H$.

The hydrostatic equation (2.6) is used in unmodified form. However, it was unnecessary to integrate it. The only purpose for which an explicit value of the air pressure is required is the computation of the saturation value of specific humidity. For this purpose, it seemed quite sufficient to use the standard pressure-height relation,

$$p = [1013.0 - 1.065 \times 10^{-3}(z + E(x, y))] \quad (2.30)$$

in which p is in millibars, z and E are in cm. The saturation value of specific humidity, q_s , may then be obtained as a function of T in °K. and z in cm. with satisfactory accuracy by a relationship adapted from Teten's formula (Haurwitz [14]):

$$q_s = \frac{3.8 \times 10^{-3}}{[1.013 - 1.065 \times 10^{-6}(z + E)]} \exp \left\{ 17.25 \left[\frac{T - 273.0}{T - 35.7} \right] \right\}. \quad (2.31)$$

The continuity equation (2.7) is simplified by neglecting the individual derivative of density. The resulting equation may be used in conjunction with equations (2.24) and (2.25) to evaluate the vertical velocity, w . Thus,

$$w(z) = -m \int_h^z \left(\frac{\partial u}{\partial x} + \frac{\partial v}{\partial y} \right) dz \quad (2.32)$$

provided that we take w to be zero at $z=h$, which it must be to very good approximation.

It is appropriate to note that if w_s is the vertical velocity in spherical coordinates, then from equation (2.3) it follows that

$$w_s = w + \hat{w} \quad (2.33)$$

in which

$$\hat{w} = \frac{dE}{dt} = m \left(u \frac{\partial E}{\partial x} + v \frac{\partial E}{\partial y} \right). \quad (2.34)$$

The form used for the thermodynamic equation (2.8) was selected because the form of the convergence of eddy heat flux term is most easily justified by use of Reynolds' averaging method in terms of potential temperature or entropy. For computational purposes, we prefer to use air temperature as the dependent variable. Additionally, we wished to use the quasi-isobaric method for computing the diabatic release of latent heat which is more simply employed when air temperature is used.

Using the definition of potential temperature

$$\theta = T \left(\frac{p}{P} \right)^{-R/c_p} \quad (2.35)$$

in which P is a reference pressure, usually 1000 mb., R is the gas constant for dry air, and c_p is the specific heat at constant pressure of dry air, one may rewrite equation (2.8) in the form

$$\frac{\theta}{T} \frac{dT}{dt} - \frac{R\theta}{c_p p} \frac{dp}{dt} = \frac{\partial}{\partial z} \left\{ \frac{\theta}{T} K_H \left[\frac{\partial T}{\partial z} + \frac{g}{c_p} \right] \right\} + \frac{\theta}{T} \frac{Q}{c_p}. \quad (2.36)$$

Since $(\partial/\partial z)(\ln \theta/T) = g/c_p T$, the equation may be expressed as

$$\frac{dT}{dt} = \frac{RT}{c_p p} \frac{dp}{dt} + \frac{\partial}{\partial z} \left\{ K_H \left[\frac{\partial T}{\partial z} + \frac{g}{c_p} \right] \right\} + \frac{Q}{c_p} + \frac{g}{c_p T} K_H \left[\frac{\partial T}{\partial z} + \frac{g}{c_p} \right]. \quad (2.37)$$

We now use two approximations to simplify the equation. First, we notice that, if dp/dt is written in spherical coordinates, one has available the frequently used approximation

$$\frac{dp}{dt} = \frac{\partial p}{\partial t} + \lambda \frac{\partial p}{\partial \lambda} + \phi \frac{\partial p}{\partial \phi} + w_s \frac{\partial p}{\partial r_e} \approx w_s \frac{\partial p}{\partial r_e}, \quad (2.38)$$

which in our coordinate system becomes (see equation (2.33))

$$\frac{dp}{dt} \approx (w + \hat{w}) \frac{\partial p}{\partial z} = -(w + \hat{w}) \rho g. \quad (2.39)$$

Secondly, we note that the last term in equation (2.37), $(g/c_p T) K_H [\partial T/\partial z + g/c_p]$, is small with the order of magnitude, 10^{-6} deg. sec.⁻¹ It was therefore neglected.

With these approximations, equation (2.37) can be written,

$$\frac{dT}{dt} = -\frac{g}{c_p} (w + \hat{w}) + \frac{\partial}{\partial z} \left\{ K_H \left[\frac{\partial T}{\partial z} + \frac{g}{c_p} \right] \right\} + \frac{Q}{c_p}. \quad (2.40)$$

The diabatic heat source denoted by Q and the rate of condensation denoted by C are related by

$$Q = L_v C \quad (2.41)$$

with L_v denoting the latent heat of vaporization. The computation of C and Q is carried out in the manner used by Fisher and Caplan [8]. As pointed out by McDonald

[20], the method involves the approximation that the phase change takes place as an isobaric process.

The formulas used to compute the coefficients K_v and K_H within the transition layer are extensions of the formulas derived using similarity theory for the layer of constant flux. Richardson's number, Ri , is defined as

$$Ri = \frac{g}{\theta} \frac{\partial \theta}{\partial z} / \left| \frac{\partial \mathbf{v}}{\partial z} \right|^2, \quad (2.42)$$

in which \mathbf{v} is the horizontal wind vector. Two turbulence regimes are recognized; viz., free and forced convection. In free convection the turbulent energy is derived principally from buoyancy forces, whereas in forced convection the energy is derived principally from the inertial forces.

If $Ri \leq -0.03$, we assume that the turbulence is of the free convection type and compute the eddy viscosity and eddy diffusivity from the relation (Priestley [24]),

$$K_v = K_H = \lambda z^2 \left| \frac{g}{\theta} \frac{\partial \theta}{\partial z} \right|^{1/2}. \quad (2.43)$$

If $Ri > -0.03$, a forced convection regime is assumed to exist and the coefficients are computed from the relation,

$$K_v = K_H = [kz(1 - \beta Ri)]^2 \left| \frac{\partial \mathbf{v}}{\partial z} \right|, \quad (2.44)$$

provided that $Ri < 1/\beta$. The values of the dimensionless parameters, β and λ , are the same as those determined empirically from observations made near the ground. We shall discuss these quantities in more detail subsequently. The values of K_H and K_v computed from equations (2.43) and (2.44) are modified so that they lie between 10^4 and $10^6 \text{ cm}^2 \text{ sec}^{-1}$. Furthermore, if $Ri > 0$ and $|\partial \mathbf{v} / \partial z| = 0$ or if $(1 - \beta Ri) \leq 0$, we set K_H and K_v equal to $10^4 \text{ cm}^2 \text{ sec}^{-1}$.

The equations (2.40), (2.9), and (2.10) require the specification of boundary and initial conditions. The initial conditions can be obtained from observational data throughout the region of integration. Lateral boundary conditions are required on the inflow boundaries for the computation of horizontal advection terms. Our assumption that the advection is zero at such inflow points involves the introduction of an error which propagates into the integration region at approximately the speed of the air motion. This error will destroy the utility of the forecasts throughout the entire region after a sufficiently long interval of time.

Boundary conditions are also required at the upper and lower boundaries of the transition layer ($z=H$ and $z=h$). On the lower boundary, we specify the eddy flux of heat and water vapor. The computation of these boundary values is carried out using the formulas derived subsequently through consideration of the properties of the layer of constant flux. On the upper boundary, q , T , and r are computed from simplified forms of the equations (2.40), (2.9), (2.10); the simplification involves the neglect at the boundary of the convergence of the

eddy flux and a one-sided approximation of the vertical derivatives of the dependent variables.

MODEL EQUATIONS FOR THE LAYER OF CONSTANT FLUX

The transition layer equations require for their solution the specification of the heat and moisture flux at the lower boundary. Also required at that level are the wind components and the eddy viscosity coefficient. These boundary conditions are provided in this model by means of a series of relations which are derived from a number of assumptions regarding the structure of the air layer in contact with the ground.

By analyses such as those given by Lumley and Panofsky [19], one can demonstrate the rationale for expecting the air near the ground to be characterized by a small vertical variation in the magnitude of the flux of momentum, heat, and vapor. To the extent possible with instruments of limited accuracy, micrometeorological observations of these eddy fluxes support these conclusions. Thus the experimental background is present for the working hypothesis that within a thin layer of air adjacent to the ground the eddy fluxes may be considered to be invariant with respect to height.

This assumption is a basis for the development of a similarity theory of the structure of the atmosphere within this layer. Accounts of the derivation of such theories are given by Monin [21], Priestley [24], and Lumley and Panofsky [19]. Our use of the results of these theoretical investigations centers in the derivation of formulas for evaluating the heat and vapor flux at the base of the transition layer.

The friction velocity, u_* , is related to the surface stress, τ_0 , and the air density, ρ , by the expression

$$|\tau_0| = \rho u_*^2. \quad (2.45)$$

Lettau [17] has shown that if one defines a geostrophic drag coefficient, C_D , by

$$C_D = u_*/G \quad (2.46)$$

in which G is the magnitude of the surface geostrophic wind, then an empirical relationship between C_D and the surface Rossby number, Ro , may be derived from observational data. Ro is defined in terms of G , the Coriolis parameter, and the surface roughness, z_0 , by

$$Ro = \frac{G}{f z_0}. \quad (2.47)$$

In Lettau's analysis, u_* was evaluated for neutral stratification. When the lapse rate departs from neutral, systematic departures from the previous estimates of C_D occur. For lapse conditions, the new drag coefficient values are about 20 percent larger and for moderately strong inversion conditions the coefficient is some 20 percent smaller, than its neutral value.

Using the data presented in Blackadar's [2] paper, we obtained by least-squares-fitting the relation,

$$u_{*N} = G(0.07625 - 0.00625 \log Ro). \quad (2.48)$$

The subscript, N , indicates that this estimate is appropriate for neutral conditions. According to Blackadar, some deviation of u_* about the value given in the equation above can be attributed to the presence of a geostrophic wind shear within the boundary layer.

The angle of deviation between the surface geostrophic wind and the wind in the layer of constant flux was shown to be a function of Ro by Blackadar [2]. Using his data, we fitted the following expression

$$\psi = a (\log Ro)^2 + b \log Ro + c \quad (2.49)$$

in which ψ is the deviation angle in degrees and the logarithm is to the base 10. The coefficients were computed to be $a = 0.625$, $b = -12.750$, and $c = 80.625$. ψ varies between 32.5° for $Ro = 10^5$ and 15.6° for $Ro = 10^{10}$. Deviations about these empirical values can be expected as a function of the stability and baroclinicity of the layer, but they have not been used in this model.

The assumption that the eddy fluxes are invariant with height permits one to write the following equations, for the surface layer,

$$K \frac{\partial s}{\partial z} = \frac{\tau_0}{\rho} = u_*^2 \quad (2.50)$$

$$K \left[\frac{\partial T}{\partial z} + \frac{g}{c_p} \right] = -\frac{H_0}{\rho c_p} = u_* \theta_* \quad (2.51)$$

$$K \frac{\partial q}{\partial z} = -\frac{W_0}{\rho} = u_* q_* \quad (2.52)$$

in which

- K is the eddy exchange coefficient
- s is the horizontal wind speed
- τ_0 is the surface stress
- H_0 is the eddy heat flux
- W_0 is the eddy vapor flux

and the quantities θ_* and q_* are constants with dimensions of temperature and specific humidity respectively.

The results of similarity theory and numerous empirical studies indicate that there are two principal turbulence regimes—forced convection and free convection—that occur in the air layer near the ground.

For a forced convection regime in which $|Ri|$ is small, it follows from the work of Monin and Obukhov (see Pandolfo et al. [22]) that the mixing coefficient may be expressed in terms of parameters of the mean flow by

$$K = [kz(1 - \beta Ri)]^2 \frac{\partial s}{\partial z}, \quad (2.53)$$

in which k is von Karman's constant, β is an empirical

constant, and Ri is the Richardson number. Ri may be expressed by the relation

$$Ri = \frac{g}{\theta} \left[\frac{\partial T}{\partial z} + \frac{g}{c_p} \right] / \left(\frac{\partial s}{\partial z} \right)^2. \quad (2.54)$$

The introduction of this forced convection formula (equation (2.53) for K) into the constant flux equations, followed by an integration from a lower level to the level $z = h$, at both of which the value of the dependent variables q and T can be assumed known, yields

$$S = s(z = h) = \frac{u_*}{k} \ln \left(\frac{h}{z_0} \right) + \frac{\theta_*}{u_*} \frac{\beta g}{\theta} (h - z_0) \quad (2.55)$$

$$T_h = T_i - \left(\frac{g}{c_p} \right) (h - z_i) + \frac{\theta_*}{k} \ln \left(\frac{h}{z_i} \right) + \frac{\beta g}{\theta} \frac{\theta_*^2}{u_*^2} (h - z_i) \quad (2.56)$$

$$q_h = q_i + \frac{q_*}{k} \ln \left(\frac{h}{z_i} \right) + \frac{\beta g}{\theta} \frac{q_* \theta_*}{u_*^2} (h - z_i). \quad (2.57)$$

The wind speed has been assumed to vanish at $z = z_0$, the roughness height. The temperature, T_i , and the specific humidity, q_i , are values at $z = z_i$, the level of the instrument shelter.

Now, in practice, predicted values of T_h and T_i are available together with an estimate of u_* . The equation (2.56) may consequently be considered to be a quadratic in θ_* . Since θ_* must vanish for neutral stratification, we can determine the appropriate root; viz.,

$$\theta_* = -\frac{u_*^2 \bar{\theta} \ln(h/z_i)}{2\beta g k (h - z_i)} \left[1.0 - \left\{ 1.0 + \frac{4\beta g}{u_*^2 \bar{\theta}} \times \left[\frac{T_h - T_i}{h - z_i} + \frac{g}{c_p} \right] \left[\frac{k(h - z_i)}{\ln(h/z_i)} \right]^2 \right\}^{1/2} \right]. \quad (2.58)$$

This formula may be evaluated from the specified data and then used to calculate S , $u_* \theta_*$, and $u_* q_*$.

It remains to demonstrate the method for computing K at $z = h$ and the values of U and V . From equations (2.50), (2.51), and (2.54) it follows that

$$Ri = \frac{g}{\theta} \frac{\theta_*}{u_*^2} \frac{K}{u_*}. \quad (2.59)$$

Furthermore, it follows from (2.50) and (2.53) that

$$\frac{K}{u_*} = kz(1 - \beta Ri). \quad (2.60)$$

If (2.60) is substituted into (2.59), one gets

$$Ri = \frac{g}{\theta} \frac{\theta_*}{u_*^2} kz(1 - \beta Ri). \quad (2.61)$$

Solving for $(1 - \beta Ri)$, we find

$$(1 - \beta Ri) = \left[1 + \frac{\beta g}{\theta} \frac{\theta_*}{u_*^2} kz \right]^{-1} \quad (2.62)$$

with the intermediate result,

$$Ri = \frac{1}{\beta} \left\{ 1.0 - \left[1.0 + \frac{\beta g}{\theta} \frac{\theta_*}{u_*^2} kz \right]^{-1} \right\} \quad (2.63)$$

noted for later reference. Finally, (2.62) can be inserted in (2.60) and K evaluated at $z=h$ to get

$$K_M = kh u_* \left[1 + \frac{\beta g}{\theta} \frac{\theta_*}{u_*^2} kh \right]^{-1}. \quad (2.64)$$

The wind components U and V can be readily derived from S , ψ , and the surface geostrophic wind components G_x and G_y . If we write

$$K_1 = S(G_x^2 + G_y^2)^{1/2} \cos \psi \quad (2.65)$$

$$K_2 = S(G_x^2 + G_y^2)^{1/2} \sin \psi \quad (2.66)$$

then

$$U = (G_x K_1 - G_y K_2) / (G_x^2 + G_y^2), \quad (2.67)$$

$$V = (G_y K_1 + G_x K_2) / (G_x^2 + G_y^2). \quad (2.68)$$

In a free convection regime the mixing coefficient is obtained from Priestley's [24] formula

$$K = \lambda z^2 \left[\frac{g}{\theta} \left| \frac{\partial T}{\partial z} + \frac{g}{c_p} \right| \right]^{1/2}. \quad (2.69)$$

This function may be introduced into the equations (2.51) and (2.52). After integration between a lower level z_i and $z=h$, at both of which the dependent variables T and q are assumed to be known, one obtains,

$$T_h = T_i - \frac{g}{c_p} (h - z_i) - \frac{3u_* \theta_*}{\lambda^{2/3} |u_* \theta_*|^{1/3}} \left[\frac{\bar{\theta}}{g} \right]^{1/3} [h^{-1/3} - z_i^{-1/3}] \quad (2.70)$$

$$q_h = q_i - \frac{3u_* q_*}{\lambda^{2/3} |u_* \theta_*|^{1/3}} \left[\frac{\bar{\theta}}{g} \right]^{1/3} [h^{-1/3} - z_i^{-1/3}]. \quad (2.71)$$

The wind profile is obtained by assuming that the mixing coefficient for heat (2.69) is 30 percent larger than that for momentum (see fig. 1, Priestley [24]) and that between z_0 and $z_0 + 1$ m. a logarithmic wind profile exists. Using these assumptions, one gets the formula

$$S = s(z=h) = \frac{u_*}{k} \ln \frac{z_0 + 1 \text{ m.}}{z_0} - \frac{3.9u_*^2}{\lambda^{2/3} |u_* \theta_*|^{1/3}} \left[\frac{\bar{\theta}}{g} \right]^{1/3} [h^{-1/3} - (z_0 + 1 \text{ m.})^{-1/3}]. \quad (2.72)$$

Equation (2.70) may be solved for $u_* \theta_*$. With that quantity, and u_* , the quantity, $u_* q_*$, can be obtained by solving equation (2.71), and the wind speed at $z=h$ obtained by evaluating equation (2.72). By simple manipulation of equations (2.69) and (2.51), one may

obtain the value of the momentum mixing coefficient at $z=h$,

$$K_M = \frac{1}{1.3} \left[\lambda^2 h^4 \frac{g}{\theta} |u_* \theta_*| \right]^{2/3}. \quad (2.73)$$

The wind components, U and V , are derived in the same way as given in equations (2.67) and (2.68).

The determination of whether the layer of constant flux is in a free or forced convection regime cannot be made through the direct computation of Ri . Indeed, it was our original plan to treat the layer of constant flux solely by means of a forced convection formulation. That plan proved to be impracticable because of the internal constraints present in the forced convection formulas. We may note for example that the value of θ_* computed from equation (2.58) will be complex, if

$$\frac{T_h - T_i}{h - z_i} + \frac{g}{c_p} < -\frac{u_*^2 \bar{\theta}}{4\beta g} \left[\frac{\ln(h/z_i)}{k(h - z_i)} \right]^2. \quad (2.74)$$

Similarly, equation (2.64) gives a negative value for K_M , if

$$\left[1.0 + \frac{\beta g}{\theta} \frac{\theta_*}{u_*^2} kh \right]^{-1} < 0. \quad (2.75)$$

If one evaluates (2.58) under the assumption that the inequality (2.74) is just balanced, one gets

$$\frac{\theta_*}{u_*^2} = -\frac{\bar{\theta}}{2\beta g} \frac{\ln(h/z_i)}{k(h - z_i)}. \quad (2.76)$$

When this value is used in equation (2.63), we find

$$Ri = \frac{1}{\beta} \left\{ 1.0 - \left[1.0 - \frac{z \ln h/z_i}{2(h - z_i)} \right]^{-1} \right\}. \quad (2.77)$$

Evaluation of (2.77) for β between 2 and 5, and with $h=50$ m. and $z_i=1$ m. yields values of $Ri < -0.03$, at or below 4.0 m. Thus the empirical limit of forced convection, $Ri = -0.03$, suggested by Priestley's analysis is internally consistent with the forced convection formulas.

The use of (2.76) in (2.75) violates the necessary sense of the inequality if the ratio, h/z_i , exceeds 7. Thus, we found that the inequality (2.75) was the more severe constraint in the application of the forced convection formulas.

The computational scheme adopted for determining the appropriate convection regime within the layer of constant flux may now be explained. We first determined if the inequality (2.74) was satisfied. If it was violated, we immediately used the free convection formulas. If it was satisfied, we computed the value of K_M from equation (2.64). If K_M was negative, we then used the free convection formulas. If K_M was positive, we then computed the heat flux ($-\rho c_p u_* \theta_*$) using both free and forced convection formulas. If the free convection value was larger, we used the free convection formulas, and conversely.

The formulas derived above involve the two non-dimensional quantities β and λ . Their appropriate values are not theoretically determinable but may be obtained through empirical data analysis. Values of β between 1 and 10 are found to be suggested in the literature. Pandolfo et al. [22] analyzed three sets of wind profiles taken in inversion conditions. They found that $\beta=3.0$ provided a good overall fit to the observations and was especially good at relatively large values of Ri . Dyer [5] has recently analyzed lapse condition observations made by Swinbank [28] and suggests that the parameter λ has a value near 1.32.

We found that the free and forced convection formulas for the heat flux could be made to yield a relationship between λ and β . The formulas were required to yield identical values at the limiting temperature gradient given in equation (2.74). The relation which resulted is,

$$\lambda = k^2 c \sqrt{\beta} \quad (2.78)$$

in which k is von Karman's constant and c is a constant dependent upon the values of h and z_i . For $h=50$ m. and $z_i=1$ m., and $k=0.38$

$$\lambda = 0.85 \sqrt{\beta}. \quad (2.79)$$

The values $\lambda=1.2$ and $\beta=2.0$ satisfy this expression and are consistent with the empirical estimates of Dyer and Pandolfo. They were consequently adopted for use.

Occasions were encountered in which the temperature difference between z_i and h became a large positive quantity. In these instances, the forced convection formula (equation (2.53)) becomes inapplicable because the factor $(1-\beta Ri)$ is negative. We therefore introduced a third set of formulas applicable to the case of a strong stable stratification. The profiles of wind, temperature, and vapor will be linear functions of height according to Monin's analysis for large values of Ri . Using a minimum value for the eddy coefficients, K_{MIN} (10^4 cm.² sec.⁻¹), the heat and vapor fluxes were calculated by the formulas,

$$H_0 = -\rho c_p K_{MIN} \left[\frac{T_h - T_i}{h - z_i} + \frac{g}{c_p} \right] \quad (2.80)$$

and

$$W_0 = -\rho K_{MIN} \frac{q_h - q_i}{h - z_i}. \quad (2.81)$$

The wind speed at $z=h$ was set equal to a fixed fraction of the surface geostrophic wind speed, G ,

$$S = s(z=h) = 0.176 G. \quad (2.82)$$

The fraction 0.176 was estimated from the Ekman spiral in which $K=10^4$ cm.² sec.⁻¹, $f=10^{-4}$ sec.⁻¹, and the assumption that the wind vanishes at $z=0$. The momentum mixing coefficient at $z=h$, K_M , was set equal to 10^4 cm.² sec.⁻¹

The procedures used to predict the temperature and specific humidity at the level of the instrument shelter z_i are now presented. For points located over water, we used $z_i=z_0$ and took the temperature equal to the climatological value of the sea surface temperature and the humidity equal to its saturation value at the sea surface temperature. For points over land, however, the surface temperature and humidity are subject to very large diurnal and interdiurnal variation. For the reasons discussed earlier, we decided against a completely physical approach to the specification of T and q at $z=0$. We adopted empirical methods which in turn required the application of the boundary values at a standard observation level, the height of the instrument shelter, z_i .

Temporal variation of the air temperature over land can be attributed to four physical processes: divergence of radiative heat flux, divergence of eddy heat flux, thermal advection, and latent heat exchange. In an effort to evaluate the first two of these processes, we used an empirical method developed by Bryan [4]. The method involves the use of the equation

$$\frac{\partial}{\partial t} T(t) = b_0 - b_1 T(t) + b_2 s(t) + b_3 r(t) \quad (2.83)$$

in which,

$$s(t) = \sin \delta \sin \phi - \cos \delta \cos \phi \cos \frac{\pi t}{12} \quad (R \leq t \leq S)$$

$$s(t) = 0 \quad (\text{otherwise}) \quad (2.84)$$

and

$$r(t) = \frac{\partial}{\partial t} [s(t)] = \frac{\pi}{12} \cos \delta \cos \phi \sin \frac{\pi t}{12} \quad (R \leq t \leq 12)$$

$$r(t) = 0 \quad (\text{otherwise}) \quad (2.85)$$

and δ is the solar declination; ϕ is the latitude; R is the local time of sunrise; S is the local time of sunset; T is the temperature; t is the time in hours after local midnight. The coefficients (b_0 , b_1 , b_2 , and b_3) are statistical quantities derived by fitting equation (2.84) to observed temperature changes. The observational data used were 10-yr. averages of the temperature change as a function of month of the year, time of day, cloudiness, wind speed, and direction. The data were provided by personnel of the 3d Weather Wing (3WW), USAF, and are discussed in a technical note by Kimball, Richardson, and Frey [15].

The data were processed so that for each month and station, three classes of data depending upon cloudiness in the categories, ceiling below 5000 ft., ceiling between 5000 and 30,000 ft., and no ceiling, were available. The basic data included average diurnal changes caused by advection. Any net diurnal temperature change—attributable to advection—was subtracted proportionately from each hourly temperature change. The available data were suitable for specifying sets of coefficients for 10

stations in the eastern United States. The coefficients were assumed to be applicable at grid points in the neighborhood of these stations.

In practice, then, we may apply the method as follows. Based on the relative humidity distribution in the boundary layer and the upper cloud condition at each time step, a decision is made as to which set of coefficients is appropriate. The current value of temperature is a known quantity as is the local time. We may therefore evaluate (2.83) to obtain the tendency due to the convergence of radiative and eddy heat flux. This is added to the tendency due to thermal advection to yield the total tendency. We neglect the possible tendency due to release of latent heat.

The model also requires the specification of the temporal variation of specific humidity at the lower boundary of the layer of constant flux. For points over water, it was assumed that the relative humidity is always 100 percent near the air-water interface. Over land, on the other hand, the low-level relative humidity depends upon the amount of available soil moisture and the complex process by which this moisture is liberated or absorbed by the soil.

In their effort to develop an analog computer for micro-meteorological use, Halstead et al. [12] were faced with the need to compute the percentage of available energy used to evaporate water. They employed a parameter, M , which is denoted as the "percent wetted area" in physiological climatology. For their problem, Halstead et al. related M to the water vapor densities as follows:

$$(\rho'_0 - \rho'_H) = M(\rho'_{SAT} - \rho'_H) \quad (2.86)$$

where ρ' denotes water vapor density; the subscript 0 denotes a measurement near the surface; the subscript H denotes a measurement some distance removed from the surface; and ρ'_{SAT} is the saturation vapor density near the surface. Using meteorological data gathered during the Great Plains field program (Lettau and Davidson [18]), Halstead et al. found that M was well correlated to measured soil moisture and that its value tended to remain constant during periods of 24 or more hours.

We have adapted this result to our problem as follows: let q_h be the specific humidity at $z=h$ and q_i the specific humidity at z_i ; finally, let q_{is} be the saturation specific humidity measured at z_i . Using measurements of these quantities made prior to the initial time of the forecast, we may compute a value of M from

$$M = (q_h - q_i) / (q_h - q_{is}) \quad (2.87)$$

Now, holding M constant through the forecast interval permits one to solve for q_i from the equation

$$q_i(t) = Mq_{is}(t) + (1 - M)q_h(t). \quad (2.88)$$

Since q_{is} is principally a function of temperature, its value may be computed from the predicted value of the surface

temperature. The value of q_h is predicted using the transition layer equation and is available at every time step for use in equation (2.88).

This then is the last result required to complete the derivation of the model equations.

3. COMPUTATIONAL MODEL

The model equations derived in section 2 were replaced by an equivalent set of equations which could be solved with an electronic computer. Involved in the transformation to a computational version of the model are the choice of suitable finite difference versions of the differential equations, the design of a logical computational sequence, and the preparation of a computer program. The latter two steps require that one first establish the discrete representation of the region within which the equations are to be solved. Finally, it is of course necessary to prepare the numerical data required as input for the computer program.

In this section, we will discuss certain details involved in the design of the computational model equations and we will indicate the procedure used in the analysis of the required input data. A description of the computational logic and the detailed computational formulas used in the numerical integrations is presented in the project report (Gerrity [10]) and is not given here because of its lack of general interest.

COMPUTATIONAL FORM OF THE MODEL EQUATIONS

The basic prediction equations are those governing T , q , and r within the transition layer. All three equations are essentially of the same form,

$$\frac{\partial Q}{\partial t} = u \frac{\partial Q}{\partial x} + v \frac{\partial Q}{\partial y} + w \frac{\partial Q}{\partial z} + \frac{\partial}{\partial z} \left[K \frac{\partial Q}{\partial z} \right] + S; \quad (3.1)$$

the boundary conditions imposed on (3.1) are of three types: (a) values of the horizontal advection of Q at inflow points of the lateral boundary; (b) value of Q at $z=H$, and (c) value of $K(\partial Q/\partial z)$ at $z=h$. Finally, initial values of Q are specified throughout the region enclosed by the lateral boundary curve and the surfaces $z=h$ and $z=H$. The values of the coefficients, u , v , w , and K as well as the source term, S , vary with all four independent variables and are to be computed from formulas which depend more or less directly upon the dependent variable Q . We may also note that the boundary values applied in (b) and (c) above also depend upon the dependent variable and its evolution in time and space. In other words, the boundary conditions imposed depend upon the solution.

Before outlining the numerical scheme for obtaining the solution to such equations, the discretization of the region of integration and the symbolic notation used must be presented.

The horizontal coordinates, x and y , are rectangular Cartesian coordinates on a polar stereographic mapping of the Northern Hemisphere. The geographical region chosen for use in our case studies is the eastern portion of the United States. We set up a square array of 100 grid points covering the greater part of that region. The points are equally spaced on the map which means that they have a regularly varying spacing on the earth's surface. Figure 1 contains a representation of the mapping of the eastern United States with the horizontal grid points indicated thereon. The distance between grid points ranges from 153 to 175 km. and increases from south to north. The vertical coordinate was replaced by grid points located at heights of 50, 100, 150, 220, 300, 400, 500, 650, 850, 1150, 1550, and 2000 m. above the ground. Temporal integration was carried out using equal time intervals of 15 min. duration.

The value of a function Q defined on the grid is indicated by the following notation,

$$Q_{l,m}^k = Q(x=x_l, y=y_m, z=z_k, t=t_n). \quad (3.2)$$

The coordinate, x_l ($l=1, \dots, 10$), runs from left to right and the points, y_m ($m=1, \dots, 10$), run from bottom to top on the map in figure 1. The coordinate, z_k ($k=1, \dots, 12$), has the values indicated earlier with $z_1=50$ m. and $z_{12}=2000$ m.

The finite difference analog to the differential equation (3.1) can now be given. The time derivative, $\partial Q/\partial t$, is replaced by a forward difference,

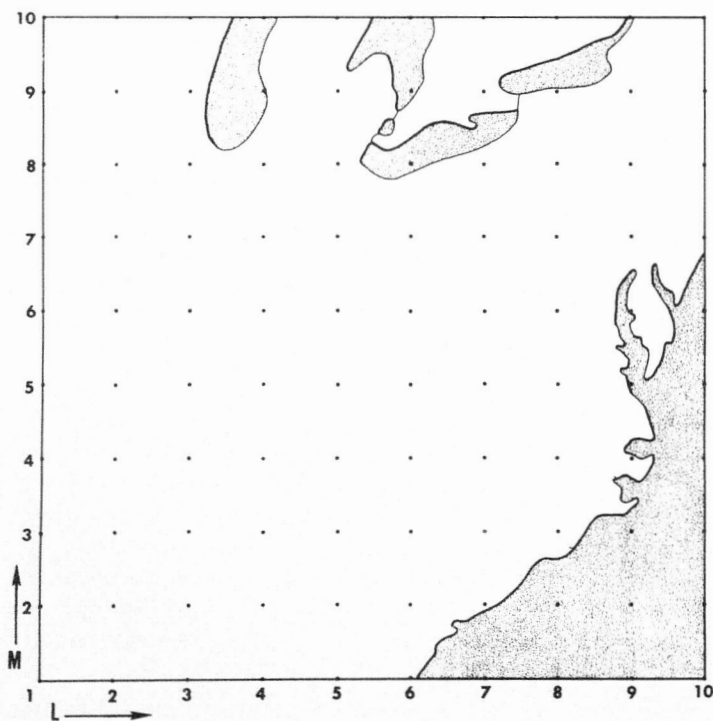


FIGURE 1.—Base map, showing horizontal grid-point array.

$$\frac{\partial Q}{\partial t} \approx \frac{Q_{l,m}^{k,n+1} - Q_{l,m}^{k,n}}{Dt}, \quad (3.3)$$

in which Dt is the time step (15 min.). The horizontal advection terms in (3.1) are approximated by the explicit upwind difference method discussed in Forsythe and Wasow [9].

For our present purpose we will assume that $u > 0$ and $v = 0$ so that the horizontal advection term in (3.1) becomes,

$$mu \frac{\partial Q}{\partial x} \approx XMS_{l,m} u_{l,m}^k \left[\frac{Q_{l,m}^{k,n} - Q_{l-1,m}^{k,n}}{Dx} \right] \quad (3.4)$$

in which $[Dx/XMS_{l,m}]$ is the grid spacing.

The vertical advection and convergence of the eddy flux terms are both approximated using implicit centered differences. The coefficients w and K , however, are computed at the current time, t_n . Using the notation, $(Dz)_k = z_k - z_{k-1}$ and $K_{l,m}^{k,n}$ equal to the value of K midway between z_k and z_{k-1} we can write the approximation,

$$\begin{aligned} -w \frac{\partial Q}{\partial z} + \frac{\partial}{\partial z} \left[K \frac{\partial Q}{\partial z} \right] \approx & \frac{Q_{l,m}^{k+1,n+1}}{(Dz)_{k+1} + (Dz)_k} \cdot \left[\frac{2K_{l,m}^{k+1,n}}{(Dz)_{k+1}} - w_{l,m}^{k,n} \right] \\ & + \frac{Q_{l,m}^{k-1,n+1}}{(Dz)_{k+1} + (Dz)_k} \cdot \left[\frac{2K_{l,m}^{k,n}}{(Dz)_k} + w_{l,m}^{k,n} \right] \\ & - \frac{2Q_{l,m}^{k,n+1}}{(Dz)_{k+1} + (Dz)_k} \cdot \left[\frac{K_{l,m}^{k+1,n}}{(Dz)_{k+1}} + \frac{K_{l,m}^{k,n}}{(Dz)_k} \right]. \end{aligned} \quad (3.5)$$

The source term, S , is approximated using data at the current time step in the case of the $(\hat{w}[g/c_p])$ -term in the thermodynamic equation. For the mass and heat exchange due to water substance phase transformation, expressed by C and Q in the water vapor and thermodynamic equations, we use the prediction-correction method (Fisher and Caplan [8]).

Using linear analysis (Richtmyer [25], [26]), one may show that the equation as approximated will be computationally stable provided that

$$Dt \leq \frac{Dx}{U}. \quad (3.6)$$

The 15-min. time step and 150-km. minimum grid spacing are well within this condition since wind speeds, U , rarely exceed 3 km. min.^{-1} . The small value of Dt was selected because the approximation was used that the coefficients (u , v , w , K , etc.), as well as the boundary conditions, are constant during the time step. This approximation might introduce large inaccuracy if the time step was extended to the limit allowed by (3.6).

The implicit structure of the approximation (3.5) requires that the difference equation applicable at each horizontal grid point be considered a coupled system of simultaneous algebraic equations for the value of Q at the next time, t_{n+1} , at each grid point $k=1, \dots, 11$. The

boundary conditions provide Q at $k=12$ and the value of $K(\partial Q/\partial z)$ at $k=1$. These equations are solved by use of a slightly modified version of the method of Gaussian Elimination described by Forsythe and Wasow [9].

ANALYSIS OF DATA

Three kinds of data are needed for the computational model: the initial values of the dependent variables, data specifying the boundary conditions, and numerical values for the several exterior parameters (e.g., Coriolis parameter, terrain elevation, etc.).

The basic dependent variables are temperature, T , and specific humidity, q . Specific moisture, r , is taken to be identical to q at the initial time; this amounts to a neglect of the liquid water content of those clouds which are already present. From the synoptic observations collected by local weather circuits, the radiosonde and surface data were extracted. The surface temperatures were plotted and analyzed. Grid-point values were interpolated from the analysis.

Temperatures at the mandatory and significant levels of the radiosonde observations were used to compute the temperature differences between the several information levels (z_k ; $k=1, \dots, 12$) of the model. The vertical temperature differences between each two levels were then plotted and analyzed. Grid-point values were extracted from the analyzed field and used in conjunction with the grid-point values of surface temperature to derive temperature values at the 12 information levels.

The temperature-dew point spread was extracted from the data at the mandatory and significant levels of the radiosonde observations. These data were interpolated to the levels z_k ; $k=1, \dots, 12$. For each level z_k the spread was plotted and analyzed. Grid-point values were extracted from the analyzed field and combined with the previously determined temperatures to provide dew-point temperatures at each grid point. The dew-point temperatures were converted to specific humidities through the application of the equation (2.31).

The analysis procedure outlined above worked reasonably well over the land portion of the region of integration. Over the oceanic portion of the region, no radiosonde data are available. Arbitrary extrapolation over the oceans of the analysis made over land is unwarranted in general and in some cases can be grossly incorrect. In practice, the climatological sea surface temperature, the surface ship observations, and the temperature and humidity patterns at 850 mb. were used as guides in estimating the structure of the air layer over the ocean. The input data used for oceanic grid points in the cases reported in section 4 are therefore highly speculative.

As outlined in section 2, certain of the boundary conditions are to be obtained from a free-air cloud prediction model. In particular the geostrophic or gradient winds at the top of the boundary layer and the amount of middle or high cloudiness are required from such a mode. For

the case studies presented subsequently, the prediction data were not available. It was necessary, therefore, to resort to the use of observed data. In a certain sense, the use of observed data for the boundary conditions would be useful in estimating the potential skill of the boundary layer model.

Practically speaking, however, upper-air data are available only at synoptic times, so that only the linear trend of the geostrophic wind during the forecast interval could be specified at the upper boundary. The upper-level cloudiness was also extracted from synoptic surface observations of cloud amount and type. The nephanalysis was made subjectively. The specification of upper cloud conditions was limited to two values characterizing conditions during the successive 6-hr. portions of the forecast interval.

No attempt was made to specify the horizontal advection on the part of the lateral boundaries experiencing flow into the region. The influence of the errors introduced on the boundary by this neglect is evident in the forecast error fields presented in section 4.

The exterior parameters needed as input are listed in table 1. The name of the parameter and the symbols used in the text are indicated. The terrain elevation, E , was obtained from data given by Berkofsky and Bertoni [3]. The ground moisture factor, M , was computed from the interpolated radiosonde data by equation (2.87). The distribution of the surface roughness parameter was obtained from data presented by Kung [16]. The radiation coefficients were derived from climatological temperature change data provided by the USAF Air Weather Service (Kimball, Richardson, and Frey [15]). The other parameters were simply computed from the map characteristics. The values used for E and z_0 are given in tables 2 and 3.

4. RESULTS OF NUMERICAL EXPERIMENTS

Numerical integration of the model equations has been carried out and analyzed for three synoptic situations,

Case A: 1200 GMT Feb. 6—0000 GMT Feb. 7, 1964

Case B: 0000 GMT Jan. 23—1200 GMT Jan. 23, 1965

Case C: 1200 GMT Jan. 24—0000 GMT Jan. 25, 1965.

In the interest of space, only Case C will be discussed at any length here, although some reference will be made to the results obtained in the other cases. More details can be obtained by reference to the project report (Gerrity [10]) and to the thesis (Gerrity [11]). In the project report, the analysis is based on the results obtained with the complete model described in section 2 above. The thesis analysis compares with the results of the complete model, those results obtained when the sensible and latent heat flux at the base of the transition layer were arbitrarily set to zero at each step in the integration. In what

TABLE 1.—Exterior parameters used in model

Name	Text symbol
Terrain elevation.....	<i>E</i>
Ground moisture factor.....	<i>M</i>
Surface roughness.....	<i>z₀</i>
Map scale factor.....	<i>m</i>
Coriolis parameter.....	<i>f</i>
Latitude.....	<i>φ</i>
Longitude.....	<i>λ</i>
Radiation coefficient.....	<i>b₀</i>
Radiation coefficient.....	<i>b₁</i>
Radiation coefficient.....	<i>b₂</i>
Radiation coefficient.....	<i>b₃</i>

TABLE 2.—Elevation of terrain (in meters) above mean sea level at various grid points given in figure 1

<i>L</i> <i>M</i>	1	2	3	4	5	6	7	8	9	10
10	367	206	227	191	227	191	191	185	70	82
9	267	327	212	191	245	191	182	167	121	182
8	261	203	197	233	258	191	348	667	369	124
7	221	179	185	245	306	282	370	385	82	15
6	252	109	118	158	273	173	606	148	9	0
5	124	91	148	239	336	439	364	124	0	0
4	70	115	183	211	330	530	221	70	6	0
3	48	70	185	203	324	136	58	15	0	0
2	115	92	52	140	93	39	18	0	0	0
1	61	52	39	61	70	21	0	0	0	0

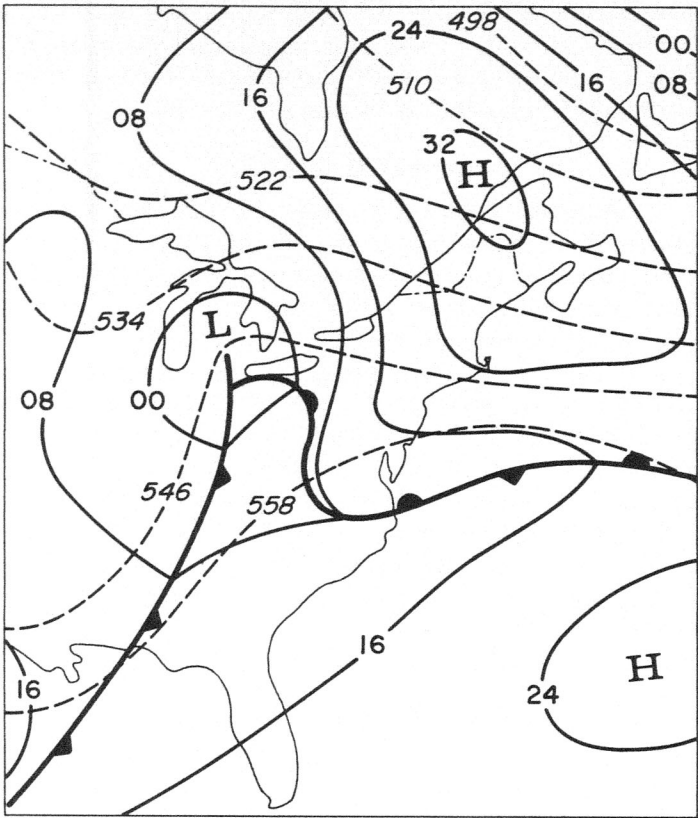


FIGURE 2.—Surface chart with 1000-500-mb. thickness at 1200 GMT January 24, 1965.

TABLE 3.—Surface roughness parameter (in centimeters) at the grid points shown in figure 1

<i>L</i> <i>M</i>	1	2	3	4	5	6	7	8	9	10
10	1	1	1	1	2	1	2	10	12	32
9	1	1	1	1	2	1	1	2	22	32
8	5	2	2	2	2	1	2	19	30	20
7	10	5	4	3	2	5	15	32	21	10
6	15	15	15	15	16	20	30	32	10	1
5	25	28	30	30	30	35	45	30	10	1
4	35	40	42	50	52	61	47	20	10	1
3	45	50	56	60	70	65	25	10	1	1
2	55	62	70	80	93	50	8	1	1	1
1	70	90	100	101	100	20	1	1	1	1

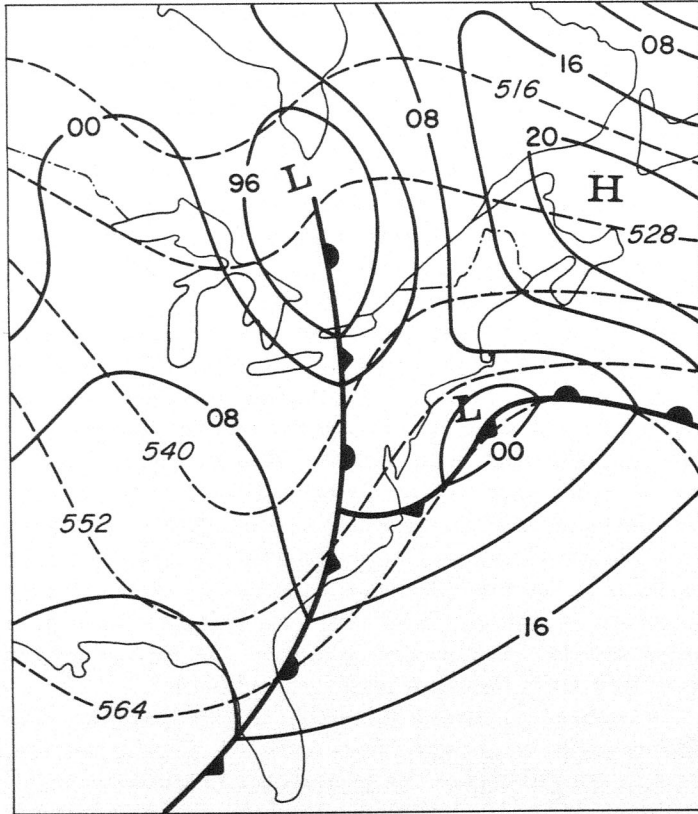


FIGURE 3.—Surface chart with 1000-500-mb. thickness at 0000 GMT January 25, 1965.

follows, the complete model is called the flux model and the alternate version, the no flux model.

Figures 2 and 3 display the synoptic patterns of sea level pressure and 1000-500-mb. thickness at the initial and verifying times of Case C. A brief description of the synoptic weather pattern follows.

At the initial time, the warm air mass was conditionally unstable. Showers were being reported in the South-eastern States and generally cloudy skies existed throughout the warm sector. The winds aloft were oriented so as to produce pronounced overrunning above the frontal

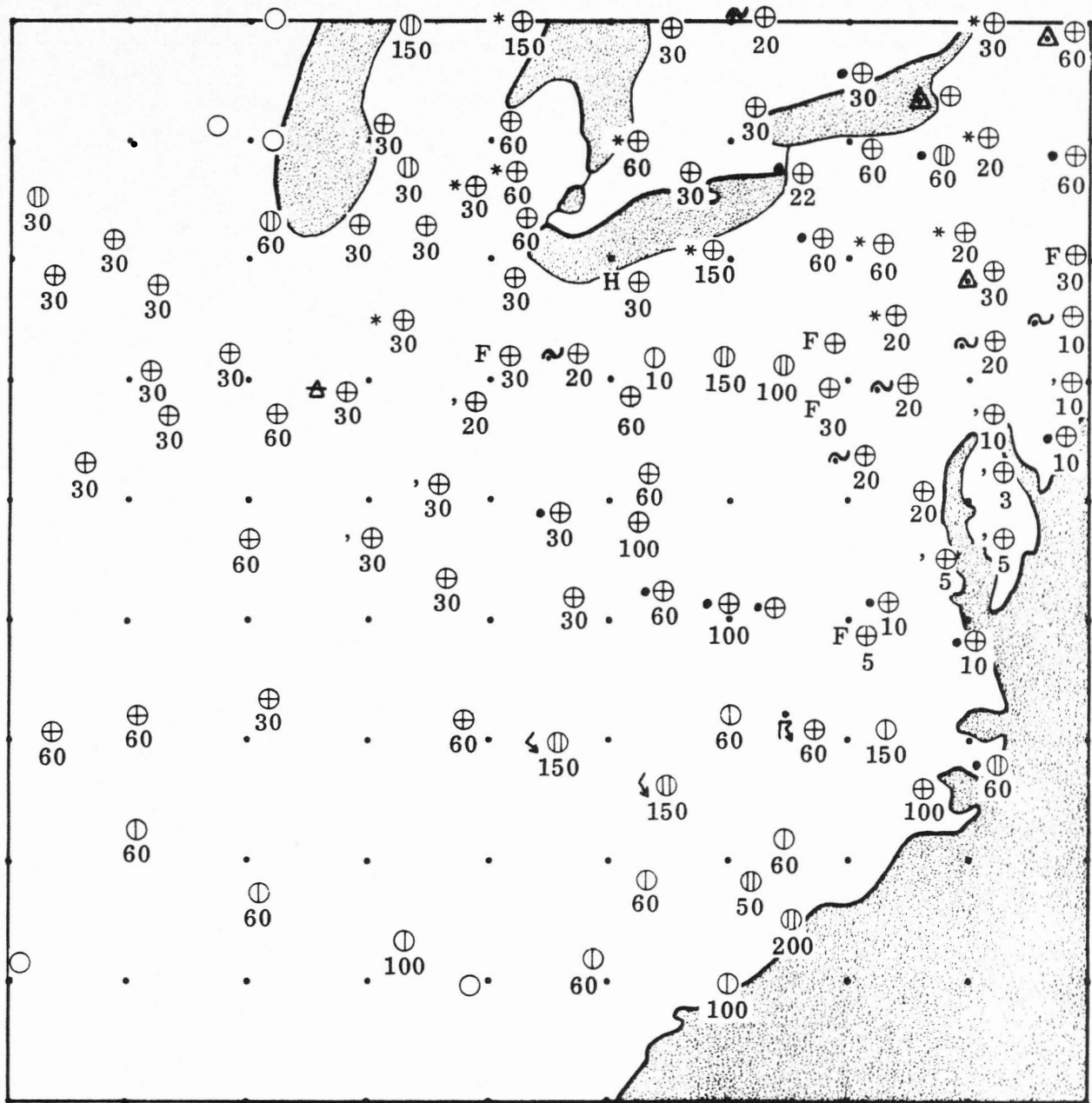


FIGURE 4.—Low cloud amount, cloud base (10's m.) and present weather observed at 0000 GMT January 25, 1965.

boundary in the Northeast. The precipitation observed in the Northeast ranged through several types: drizzle, sleet, and snow. Freezing drizzle was the predominant form of precipitation reported to the north of the low center. To the west of the cold front, the air mass was unstable beneath the frontal surface, but showers were observed only to the north of central Tennessee. In Mississippi, the Jackson radiosonde indicated subsidence above the 820-mb. level. During the forecast interval, the low center in Michigan moved northeastward over Lake Huron deepening some 7 mb. by 2100 GMT January 24. During the last 3 hr. of the forecast interval, the

Low filled abruptly as a secondary developed rapidly at 40° N., 72° W. The cold front moved uniformly eastward and by 1200 GMT occluded the warm sector from Virginia northward. Throughout the period, precipitation of mixed form fell on the northeastern section. A band of showers remained active along the southeastern coast and moved offshore as the front approached. Behind the cold front, the showers diminished in areal extent up to 2100 GMT. There was however, an isolated band of precipitation active in Tennessee and another to the east of Lake Michigan. During the 3-hr. period, 2100 to 0000 GMT, precipitation developed over Indiana and Ohio.

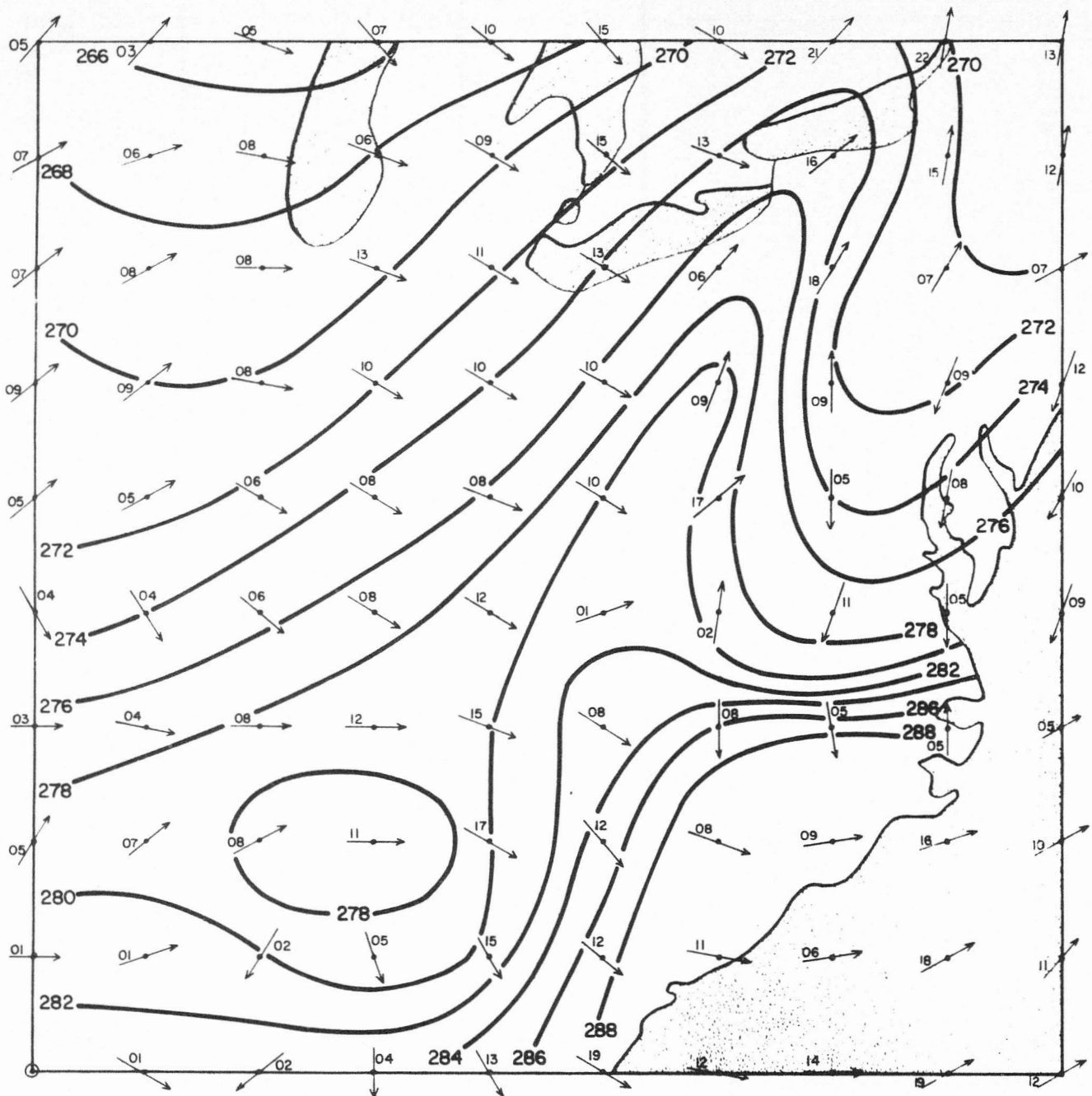


FIGURE 5.—Surface isotherms ($^{\circ}\text{K.}$) and 50-m. wind field diagnosed by model from data observed at 0000 GMT January 25, 1965.

Thunderstorms were reported in the vicinity of the point of the occlusion. The subsidence reported over Jackson intensified during the period, being symptomatic of the fair skies reported over the southern tier of States at the verifying time.

In figure 4, the low cloud and present weather observed at 0000 GMT January 25, 1965 are spotted on the base map displaying the grid points used in the computations. The low cloud amount is indicated by airways code

symbols; the reported bases of the low cloud are shown in tens of meters. In figure 5, the surface isotherms analyzed from observations at 0000 GMT January 25 are shown. The 50-m. wind diagnosed by means of the model wind formulas from observed radiosonde data is displayed. An arrow is used to indicate direction and numerals to show speed in meters per second. The corresponding data predicted by the model are given in figure 6. The temperature changes observed and pre-

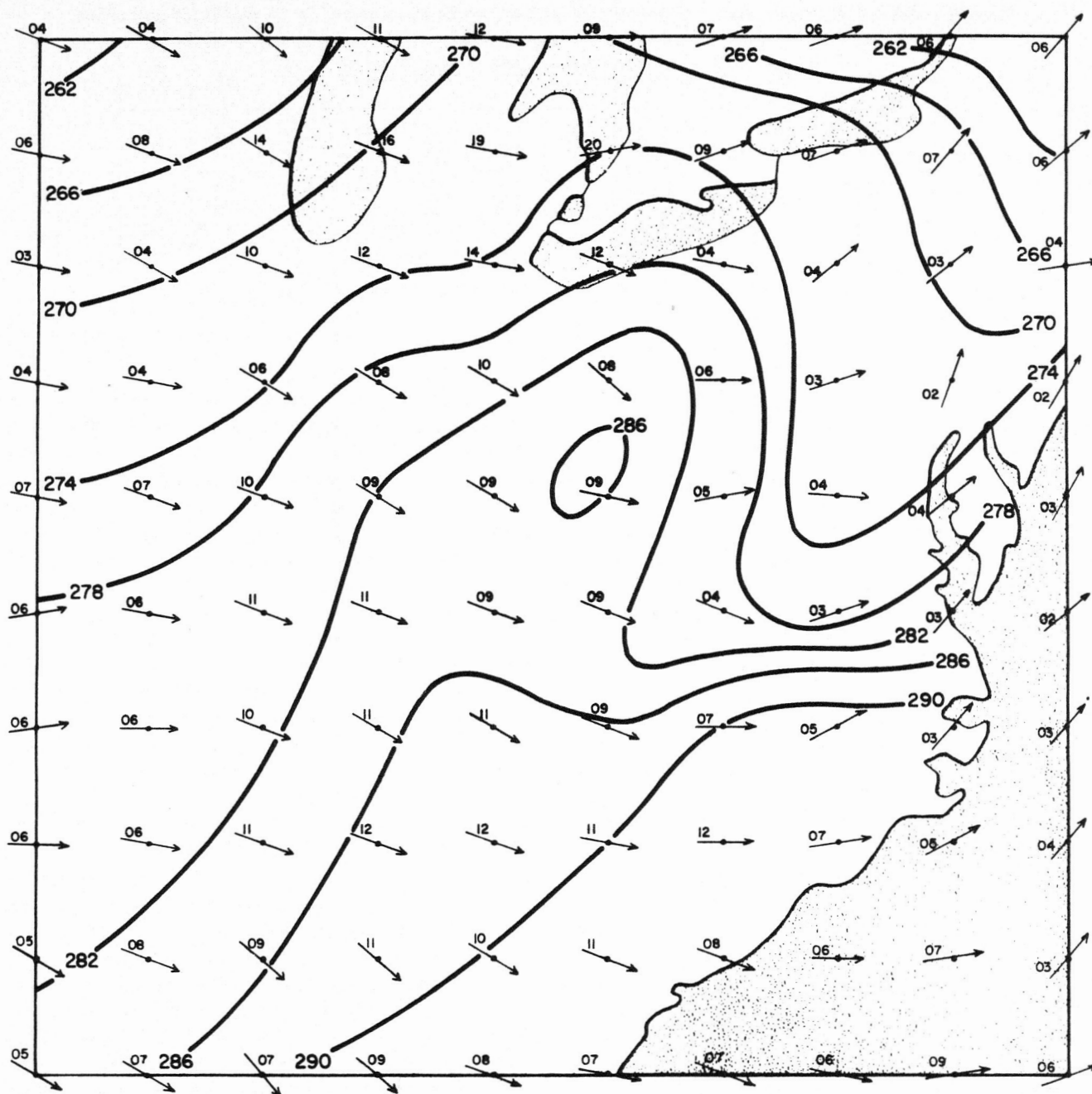


FIGURE 6.—Surface isotherms ($^{\circ}\text{K.}$) and 50-m. wind field predicted by model for 0000 GMT January 25, 1965.

dicted for the 500-m. level are presented in figure 7. The two patterns are well correlated. Especially good accuracy was obtained in the vicinity of Lake Erie, in marked contrast to the excessive warming predicted in the northeastern section. The latter error is related to the failure of the model to predict the circulation associated with the off-shore low.

The experience obtained in all of the experiments has been less satisfactory than desired in the computation

of thermal advection in advance of warm fronts. One possible cause of this is the use in the current model of a constant value of the thermal wind in each vertical. The variation in thermal wind generally noted when a frontal boundary is penetrated, should be susceptible to modelling of at least a rudimentary character, and ought to be introduced in subsequent experimental work.

Table 4 provides a statistical summary of the accuracy of the temperature forecasts in the three case studies.

TABLE 4.—Selected statistical measures of the accuracy of 12-hr. temperature forecasts for the interior 36 grid points

Case	Height	rms error "flux"	rms error "no- flux"	rms error persist.	Temp. change R	AAE "flux"	AAE persist.	Avg. fct. ΔT	Avg. obs. ΔT	$\sigma_{\Delta T}$ fct.	$\sigma_{\Delta T}$ obs.
A	500 m.	2.15	2.41	4.16	0.80	1.74	3.53	-2.3	-2.3	2.2	3.4
	1150 m.	2.20	2.27	5.21	.89	1.75	4.45	-2.3	-3.0	3.1	4.2
	2000 m.	3.26	3.45	6.20	.86	2.64	5.36	-1.1	-1.2	3.6	6.0
B	500 m.	3.65	3.78	2.31	.27	2.58	1.88	1.7	-0.4	2.7	2.3
	1150 m.	2.65	2.66	2.23	.21	2.07	1.80	1.4	0.9	2.1	2.0
	2000 m.	2.37	2.32	2.14	.27	1.98	1.85	0.5	0.6	1.9	2.0
C	500 m.	4.01	2.92	7.37	.73	3.22	6.72	-3.8	-6.7	3.6	3.0
	1150 m.	2.81	2.73	8.33	.65	2.17	7.86	-6.4	-7.9	3.0	2.8
	2000 m.	2.87	2.92	7.23	.46	2.19	6.64	-6.0	-6.6	2.3	2.9

To avoid overweighting errors incurred at the lateral boundaries, the statistics were compiled only for the interior 36 grid points. It will be noted that the root mean square (rms) error and average absolute error (AAE) are larger at 500 m. than at the higher levels in the flux model and should be contrasted with the no-flux model result. This point will be discussed subsequently. The correlation coefficient, R , the average value and standard deviation, σ , of the temperature change forecast (ΔT) are also shown in the table. The values of rms and AAE are also given for a persistence (zero temperature change) forecast. It must be remarked that the poor statistical results for Case B are largely the result of a sizable error (8° C. at 500 m.) committed just to the north of a quasi-stationary front. That error is attributable to the thermal wind representation used in the present version of the model.

In figure 8, the net flux of sensible heat into the transition layer during the forecast interval is depicted. If this heat were transformed into internal energy entirely within the 2-km. deep transition layer, it would have produced about a 2° C. mean temperature increase for each 100 langley. A comparison of figures 7 and 8 indicates that there is a qualitatively good relationship between the sensible heat input and the over-prediction of temperature in the post-cold-frontal region. This provides some indication that the sensible heat flux was overestimated. A further reference to figures 5 and 6 suggests that the overestimate is related to an underestimate of advective cooling at the instrument shelter level or to a tendency for the empirical method for estimating "radiation" temperature change to predict overly great surface warming.

Figure 9 shows the predicted net flux of latent heat (water vapor) into the transition layer during the forecast period. In figure 10, the computed heat of condensation realized within the transition layer is shown. The latter field was computed by noting the magnitude of the excess of the predicted specific moisture above the saturated value of specific humidity at the verification time. It would appear that the moisture added to the air by evaporation is not involved in the condensation process in a significant way. This, however, raises a question. How

is cloudiness to be specified, when the field parameters are temperature, specific humidity, and specific moisture?

From the outset of this model development, it has been considered likely that, in operational application, empirical rules would be available for interpreting the predicted quantities in terms of cloudiness. The development of such rules requires a suitably large sample of forecasts made with the model. For the present, it was necessary to employ empirical rules developed from concurrent observations of relative humidity, RH, and cloud amount. The relationship presented in a paper by Smagorinsky [27] was adopted. This relationship indicates that scattered low cloudiness occurs if 62 percent \leq RH \leq 77 percent; broken low cloudiness occurs if 77 percent \leq RH \leq 87 percent; overcast low cloudiness occurs if RH $>$ 87 percent, and it is accompanied by precipitation if RH $>$ 90 percent. The relative humidities used in deriving this relationship were measured at 850 mb. In the interpretation of the model forecasts, the relationship was assumed to apply between RH and cloud amount at each gridpoint within the transition layer. Figure 11 was prepared from the flux model forecast values of relative humidity and temperature. The precipitation type was based on the temperature structure at and below the levels at which RH $>$ 90 percent. The base and top of the cloudiness is indicated in tens of meters. This diagnosis was used in conjunction with the observational data in figure 4 to compile a contingency table of the amount of low cloudiness forecast and observed at the interior 36 gridpoints. A similar analysis was made in the other case studies and for the no-flux forecasts. The results are given in tables 5 through 10. It may be noted that the percentage of "hits" is higher for the flux than the no-flux forecasts. The total number of verification points varies because, at a few points, the observed data did not permit a reasonably confident interpolation of observed cloudiness to be made.

To conclude the discussion of the results obtained in Case C, an example of the temporal evolution of the forecast above a specific horizontal grid point will be shown. The grid point selected is $L=6$, $M=6$, which is located in the vicinity of the radiosonde observation station at Huntington, W. Va. Originally located within the warm

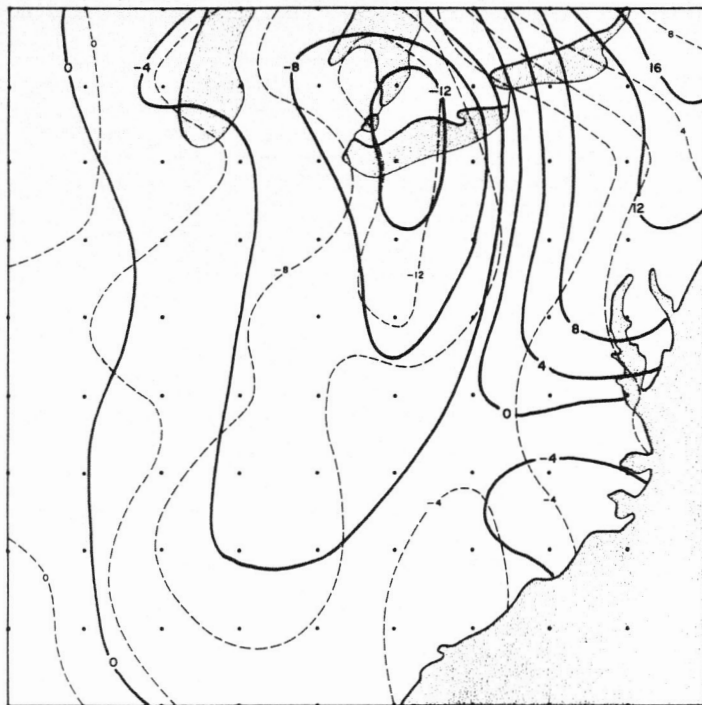


FIGURE 7.—Predicted (solid) and observed (dashed) 12-hr. temperature changes ($^{\circ}\text{K.}$) at 500 m.

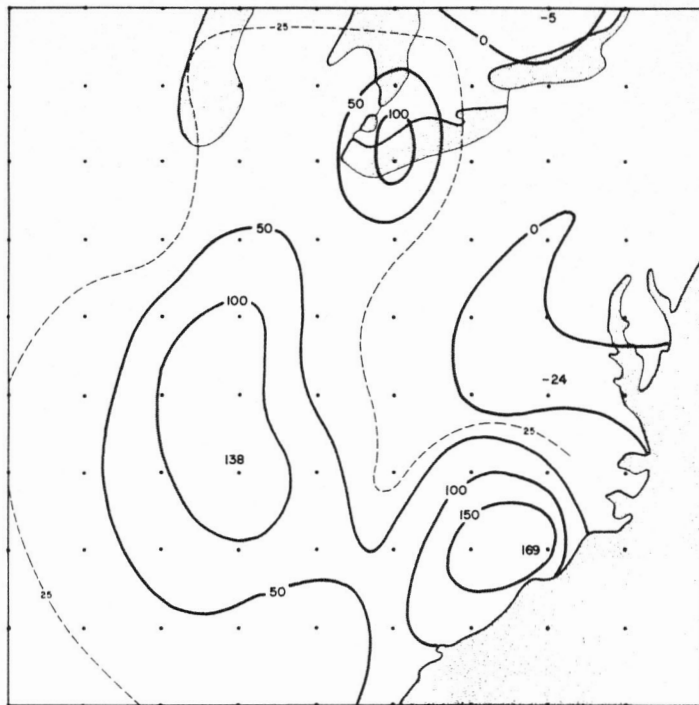


FIGURE 9.—Net eddy flux of latent heat (langleys) into transition layer during 12-hr. forecast interval.

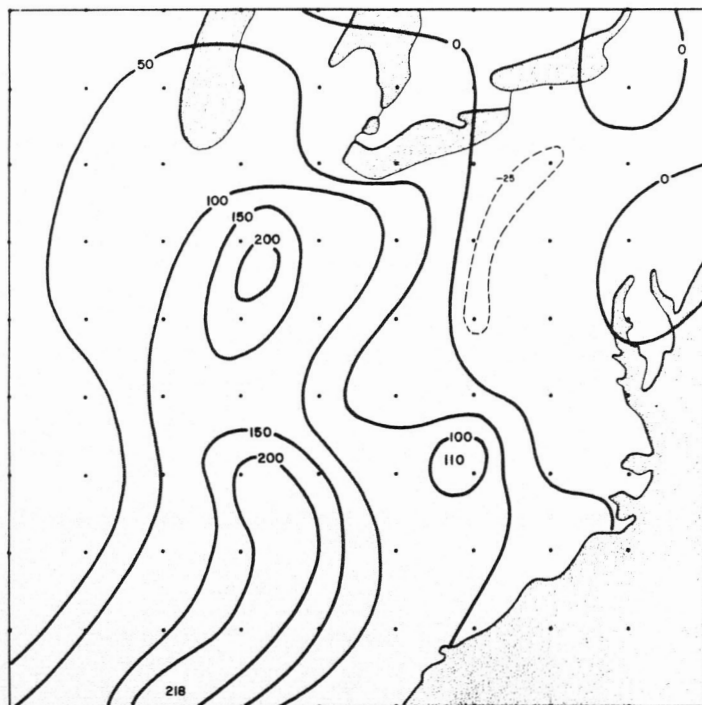


FIGURE 8.—Net eddy flux of sensible heat (langleys) into transition layer during 12-hr. forecast interval.

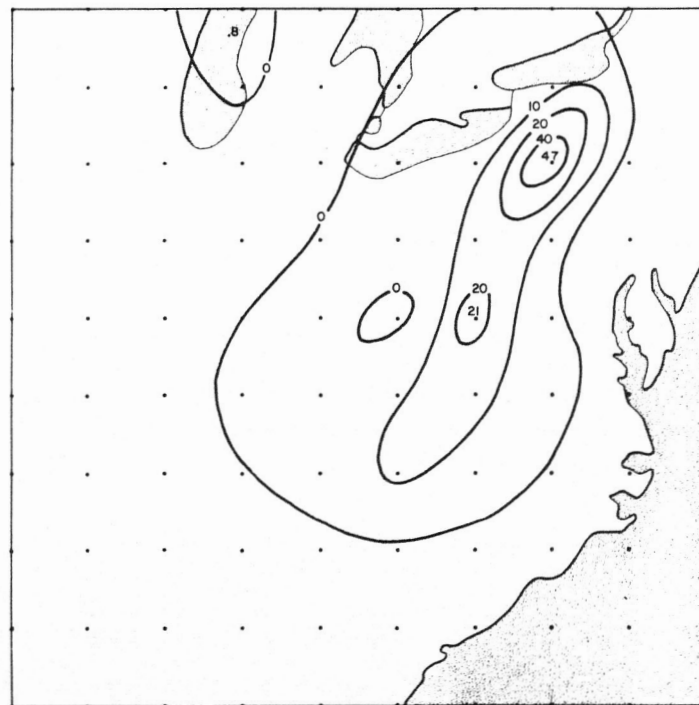


FIGURE 10.—Net heat of condensation (langleys) realized within transition layer during 12-hr. forecast interval.

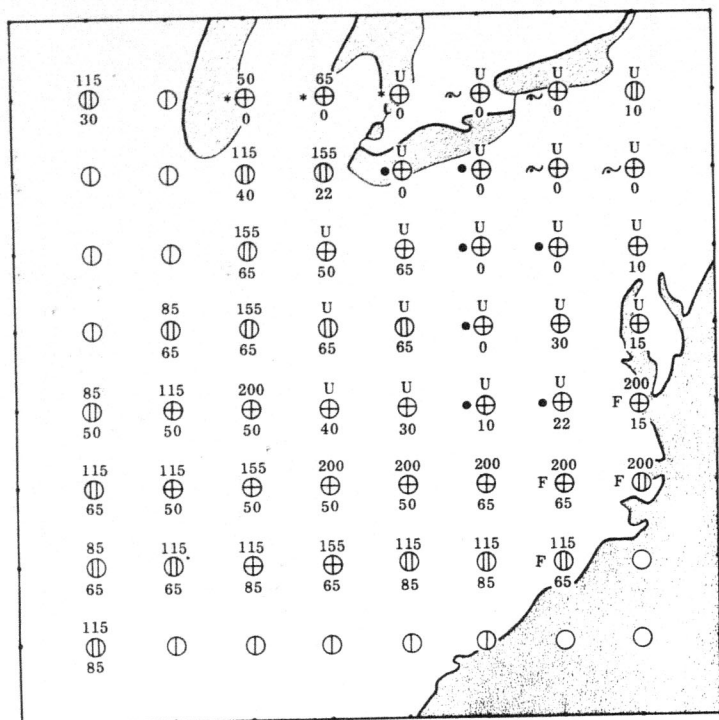


FIGURE 11.—Grid-point distribution of low cloud amount, cloud bases and tops (10's m.), and precipitation type diagnosed from flux model forecast valid at 0000 GMT January 25, 1965.

air mass on the NMC 3-hr. analysis, Huntington was passed by the cold front about 1700 GMT January 24.

In figure 12, a vertical-time section above $L=6$, $M=6$ displays the predicted isotherms and contours of relative humidity. The heavy dashed line depicts the top of the mixed layer, which was defined as the level at which the coefficient of eddy conductivity begins to decrease with height. Along the base of the chart, the computed values of friction velocity, instrument shelter temperature, and both sensible and latent heat flux are given. Notice that the development of a turbulence inversion is predicted to commence at approximately the same time that the cold front was observed to pass the nearby station.

Figure 13 shows the horizontal and vertical wind profiles at the zeroeth (00), sixth (06), and twelfth (12) hours of the forecast period. In the hodograph, the end points are labeled with the gridpoint index for which they

TABLE 5.—Verification of "flux" forecast of low cloudiness for case A

		Observed			
		⊕ or precip.	⊕	⊖ or ○	Total
Forecast	⊕ or precip.-----	16	3	3	22
	⊕-----	4	4	3	11
	⊖ or ○-----	0	1	0	1
	Total-----	20	8	6	34

TABLE 6.—Verification of "no flux" forecast of low cloudiness for case A

		Observed			
		⊕ or precip.	⊕	⊖ or ○	Total
Forecast	⊕ or precip.-----	12	1	2	15
	⊕-----	6	5	3	14
	⊖ or ○-----	2	2	1	5
	Total-----	20	8	6	34

TABLE 7.—Verification of "flux" forecast of low cloudiness for case B

		Observed			
		⊕ or precip.	⊕	⊖ or ○	Total
Forecast	⊕ or precip.-----	14	3	0	17
	⊕-----	4	3	0	6
	⊖ or ○-----	2	2	6	10
	Total-----	20	7	6	33

TABLE 8.—Verification of "no flux" forecast of low cloudiness for case B

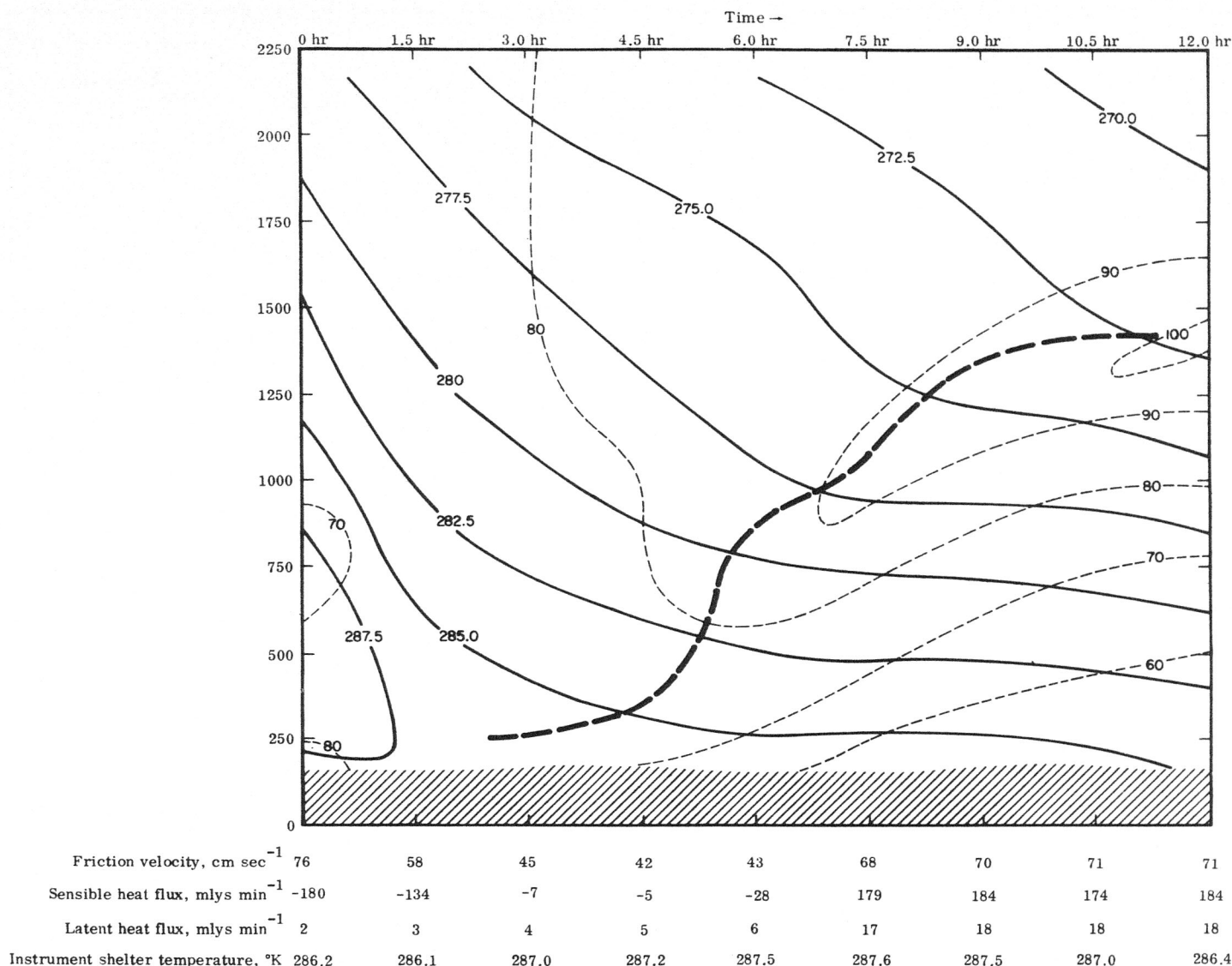
		Observed			
		⊕ or precip.	⊕	⊖ or ○	Total
Forecast	⊕ or precip.-----	9	1	0	10
	⊕-----	8	3	0	11
	⊖ or ○-----	3	3	6	12
	Total-----	20	7	6	33

TABLE 9.—Verification of "flux" forecast of low cloudiness for case C

		Observed			
		⊕ or precip.	⊕	⊖ or ○	Total
Forecast	⊕ or precip.-----	17	2	4	23
	⊕-----	7	2	2	11
	⊖ or ○-----	1	1	0	2
	Total-----	25	5	6	36

TABLE 10.—Verification of "no flux" forecast of low cloudiness for case C

		Observed			
		⊕ or precip.	⊕	⊖ or ○	Total
Forecast	⊕ or precip.-----	13	2	3	18
	⊕-----	8	0	3	11
	⊖ or ○-----	4	3	0	7
	Total-----	25	5	6	36

FIGURE 12.—Time cross-section of forecast data at grid point $L=6$, $M=6$.

apply (see section 3). It is clear that the baroclinicity of the boundary layer is significant. The relatively complex profile of the vertical velocity at the initial time is the result of the superposition of \hat{w} , the "terrain"-induced component, which is negative, and the "frictional" component, w , which is positive. After the passage of the front, the frictional component of the vertical velocity diminished to nearly zero. The profile at the later times is largely due to the \hat{w} component.

Finally, figures 14 and 15 indicate the temperature and specific humidity profiles predicted by the flux and no-flux versions of the model at grid point $L=6$, $M=6$. Also shown are the initial and verifying profiles observed at Huntington (HTW). It is clear that the error in the instrument shelter temperature resulted in an overpredic-

tion of the sensible heat flux. The flux model, reacting to this energy source, distributed the heat upward, resulting in an excessively high temperature forecast in the lower 850 m. The no-flux model, on the other hand, was arbitrarily decoupled from the eddy flux. The predicted temperatures are somewhat too low. These results indicate that additional experimentation is necessary in order to isolate the deficiencies in the current scheme for computing the instrument shelter temperature. Among the possibilities in this regard, we may indicate the following: (1) the use of observed cloudiness in the analysis of initial data to insure the use of the appropriate set of empirical coefficients at the start of the computation; (2) the computation of the empirical coefficients for more surface stations; and (3) the "tuning" of the formulas for surface advection and eddy flux.

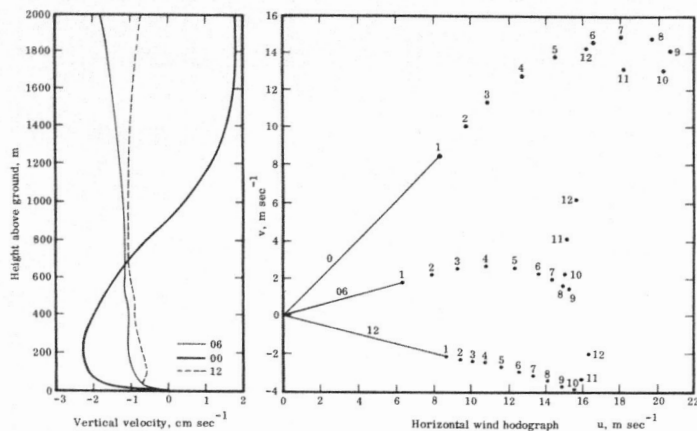


FIGURE 13.—Horizontal and vertical winds predicted for grid point, $L=6$, $M=6$.

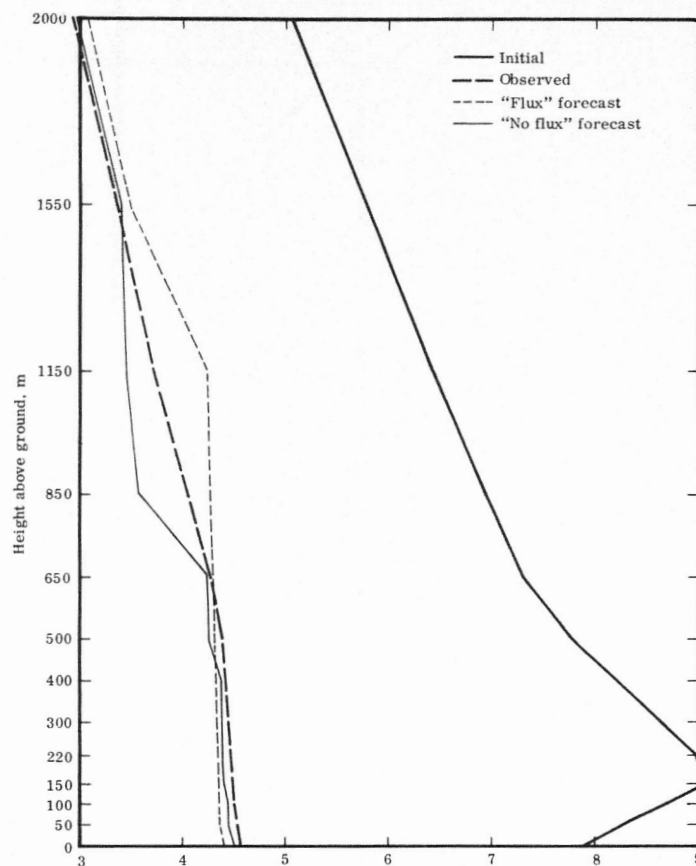


FIGURE 15.—Specific humidity profiles predicted for grid point $L=6$, $M=6$ by the flux and no-flux models. Also shown are the initial and verifying profiles observed at Huntington, W. Va.

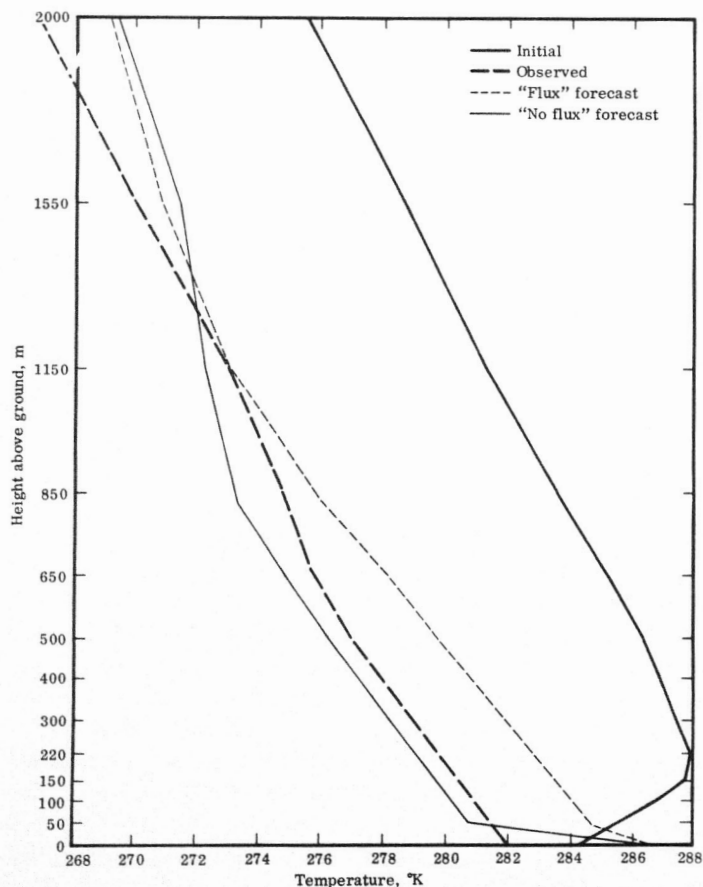


FIGURE 14.—Temperature profiles predicted for grid point $L=6$, $M=6$ by the flux and no-flux models. Also shown are the initial and verifying profile observed at Huntington, W. Va.

5. CONCLUSIONS

The results obtained in the synoptic case studies indicate that the physical model presented here may prove to be useful as an operational method for low cloud prediction in data-dense regions. Other applications might also be considered for a model of the type presented in view of the demonstrated capability of such a model to predict the low-level profiles of meteorological parameters with significant realism. Considerable operational development may well be anticipated however, before the approach embodied in this model can be expected to compete effectively with other forecast techniques.

Based upon the results obtained here, several logical developments may be suggested to improve and extend the model formulation.

Most importantly, the scheme used for computing the temperature at instrument shelter level needs to be improved. In this regard, it is considered desirable that a quasi-empirical approach for the estimation of the combined influence of radiative and sensible heat flux convergence be retained. It would also be valuable to develop a scheme for identifying significant variations in the

thermal wind, so that the horizontal wind may be computed more accurately in vertical columns which contain warm frontal inversions.

Given the availability of bigger computer storage, it seems feasible to introduce the precipitation process into the model. This modification is desirable in order to provide a basis for computing the increase in the relative humidity in the subcloud layers in response to the evaporation of the precipitation. It is desirable, for this purpose, that the precipitation rate from middle cloud layers be available. A "moist", free-air model is a prerequisite for this function.

Finally, to the extent that the radiative heat flux from cloud surfaces is important for maintaining thermal stratification, it would be desirable to add this process to the model. There is a logical difficulty in effecting this modification because of the uncertainty in specifying cloudiness. It may be sufficient to introduce this process only in the case of overcast cloudiness. A systematic use of cloud observations in the analysis of the initial state, together with the use of estimates of cloud liquid water content is called for.

The operational implementation of this model and, in fact, the conduct of further developmental experimentation would be made more efficient if a good automated technique for objective analysis of the initial state were developed. The manual analysis techniques employed in the reported work required an inordinate effort. In this connection, it may be worthwhile noting that the use of the model as part of the analysis process, e.g., to compute initial tendencies, vertical motions, etc., has a potential application in the diagnosis of smaller-scale, synoptic weather phenomena.

ACKNOWLEDGMENTS

This paper is based in large measure upon work conducted with the support of the U.S. Air Force under Contract AF19(628)-3437 with the United Aircraft Corporation, and subcontract 15107 with The Travelers Research Center, Inc. It is an abridgment of a thesis submitted to the Department of Meteorology and Oceanography of New York University in partial fulfillment of the requirements for the Ph. D. degree. Financial support during the preparation of the thesis was generously provided by The Travelers Research Center, Inc.

To the members of his thesis committee, Professors B. Davidson, R. Deland, and K. Ooyama, the author wishes to express his gratitude for their advice and encouragement. To Messrs. R. Chu, R. Metcalf of TRC, and Mrs. L. Ruffeth of UAC are due sincere thanks for their skillful assistance in preparing the data and programs used in this work. Finally, to my friend and colleague, Dr. J. Pandolfo of TRC, is due the most sincere gratitude for his continued interest and most especially for his encouragement throughout this work.

REFERENCES

1. G. 'Arnason, J. P. Gerrity, Jr., and A. Pavlowitz, "Large-Scale Cloud Prediction: A Survey and an Appraisal," Technical Report 7045-45, Contract AF19 (626)-16, The Travelers Research Center, Inc., 1963.
2. A. K. Blackadar, "The Vertical Distribution of Wind in a Baroclinic Adiabatic Atmosphere Boundary Layer," Dept. of Meteorology, Pennsylvania State University, 1963 (Unpublished).
3. L. Berkofsky and E. A. Bertoni, "Topographic Charts at One-Degree Intersections for the Entire Earth," *GRD Research Notes* No. 42, Air Force Cambridge Research Laboratories, Bedford, Mass., 1960, 43 pp.
4. J. G. Bryan, "Short-Range Hour by Hour Forecast of Temperature by Projecting the Characteristic Curve with Constants Fitted by Immediately Preceding Data," The Travelers Research Center, Inc., 1964 (Unpublished).
5. A. J. Dyer, "The Flux-Gradient Relation for Turbulent Heat Transfer in the Low Atmosphere," *Quarterly Journal of the Royal Meteorological Society*, vol. 91, No. 388, 1965, pp. 151-157.
6. W. P. Elliott and D. W. Stevens, "A Numerical Method for Computing Radiative Temperature Changes Near the Earth's Surface," *GRD Research Notes* No. 69, Air Force Cambridge Research Laboratories, Bedford, Mass., 1961, 21 pp.
7. M. Estoque, "A Numerical Model of the Atmospheric Boundary Layer," *Journal of Geophysical Research*, vol. 68, No. 4, Feb. 15, 1963, pp. 1103-1113.
8. E. L. Fisher and P. Caplan, "An Experiment in Numerical Prediction of Fog and Stratus," *Journal of the Atmospheric Sciences*, vol. 20, No. 5, Sept. 1963, pp. 425-437.
9. G. Forsythe and W. Wasow, *Finite Difference Methods for Partial Differential Equations*, John Wiley & Sons, Inc., New York, 1960.
10. J. P. Gerrity, Jr., *A Physical Low-Cloud Prediction Model*, ESD-TR-65-476, 433L System Program Office, ESD, AFSC, L. G. Hanscom Field, Bedford, Mass., 1965.
11. J. P. Gerrity, Jr., *A Physical-Numerical Model for the Prediction of Synoptic-Scale Low Cloudiness*, Ph.D. Thesis, Dept. of Meteorology and Oceanography, New York University, N.Y., 1966.
12. M. H. Halstead, R. L. Richman, W. Covey, and J. D. Merryman, "A Preliminary Report on the Design of a Computer for Micrometeorology," *Journal of Meteorology*, vol. 14, No. 4, Aug. 1957, pp. 308-325.
13. G. J. Haltiner and F. L. Martin, *Dynamical and Physical Meteorology*, McGraw-Hill Book Co., New York, 1957, 470 pp.
14. B. Haurwitz, *Dynamic Meteorology*, McGraw-Hill Book Co., New York, 1941.
15. S. J. Kimball, N. N. Richardson, and D. H. Frey, *The Use of Diurnal Temperature and Dew-Point Curves*, Scientific Services, Technical Note No. 7, Headquarters 3d Weather Wing, Offutt Air Force Base, Nebraska, 1964.
16. E. C.-T. Kung, *Climatology of Aerodynamic Roughness Parameter and Energy Dissipation in the Planetary Boundary Layer over the Northern Hemisphere*, Annual Rpt., Contract CA-36-039-A, C-00878, Dept. of Meteorology, University of Wisconsin, 1963.
17. H. H. Lettau, "Wind Profile, Surface Stress and Geostrophic Drag Coefficients in the Atmospheric Surface Layer," *Advances in Geophysics*, vol. 6, Academic Press, N.Y., 1959, pp. 241-257.
18. H. H. Lettau and B. Davidson, *Exploring the Atmosphere's First Mile*, 2 vols., Pergamon Press, New York, 1957.
19. J. L. Lumley and H. A. Panofsky, *The Structure of Atmospheric Turbulence*, John Wiley and Sons, Inc., New York, 1964.
20. J. F. McDonald, "The Saturation Adjustment in Numerical Modeling of Fog," *Journal of the Atmospheric Sciences*, vol. 20, No. 5, Sept. 1963, pp. 476-478.
21. A. S. Monin, "Struktura Atmosfernoi Turbulentnosti," [Structure of Atmospheric Turbulence], *Teoriia Veroiatnostei i ee Primeneniia*, vol. 3, No. 3, 1958, pp. 285-317.
22. J. P. Pandolfo, D. S. Cooley, and E. A. Newburg, *Preliminary*

- Investigations of Numerical Models for the Short-Period Prediction of Wind, Temperature, and Moisture in the Atmospheric Boundary Layer*, Final Rpt., 7047-80, The Travelers Research Center, Inc., 1963.
23. J. P. Pandolfo, D. S. Cooley, and M. A. Atwater, *The Development of a Numerical Prediction Model for the Planetary Boundary Layer*, Final Rpt., 7465-174, Contract Cwb-10960, The Travelers Research Center, Inc., 1965.
24. C. H. B. Priestley, *Turbulent Transfer in the Lower Atmosphere*, The University of Chicago Press, Chicago, 1959.
25. R. D. Richtmyer, *Difference Methods for Initial Value Problems*, John Wiley & Sons, Inc., New York, 1957.
26. R. D. Richtmyer, *A Survey of Difference Methods for Non-Steady Fluid Dynamics*, NCAR Tech. Notes 63-2, National Center for Atmospheric Research, Boulder, Colo., 1962.
27. J. Smagorinsky, "On the Dynamical Prediction of Large-Scale Condensation by Numerical Methods," *Geophysical Monograph No. 5: Physics of Precipitation*, American Geophysical Union, Washington, D.C., 1960, pp. 71-78.
28. W. C. Swinbank, "The Exponential Wind Profile," *Quarterly Journal of the Royal Meteorological Society*, vol 90, No. 384, Apr. 1964, pp. 119-135.

[Received January 17, 1967; revised March 20, 1967]